# Space-borne atmosphere measuring UV spectrometer development and study on retrieval algorithm

（衛星搭載大気観測紫外分光計の開発とリトリーバルアルゴリズムに関する研究）

Akihiko KUZE

久世暁彦

# 概　要

　　衛星からの大気観測では長期の全球観測が可能で、同一機器により多くのデータを取得できるという長所がある。また近年の地球環境問題により、観測の高精度化や大気物理・化学過程の解明の社会的要請が高まっている。特に人間活動の影響を直接うける対流圏の観測は重要度を増しているが、衛星軌道からの観測は高高度大気の方が有利であり、対流圏に関しては新たなアルゴリズムの開発および装置の高性能化が必要となる。一方紫外波長域は、陸・海とも地表面アルビードが小さく、さらに太陽光の大気進入高度が波長により異なるため、高度情報を含む大気観測に有利である。この波長帯には $O_3$、$NO_2$、$SO_2$ などの大気分子の吸収があり、エアロソルには吸収特性をもつものがある。これらの物理量を導出するアルゴリズムを開発し、観測を実現する衛星搭載装置を設計・製作し、その性能の実証評価を行った。

　　従来型の機器の課題を明らかにするため、ADEOS 衛星に搭載された TOMS　$O_3$ 全量および地表面アルビードの導出方法を行った。従来の解析では地上・ゾンデ観測をもとに導出 $O_3$ 量に対し補正を必要としたが、今回、装置関数モデルを解析にとりいれることで衛星データ単独で $O_3$ 全量を導出できるようになった。しかし、分光分解能が十分でない、波長シフトがあるなどの問題があるため、次世代の機器への要求を明確にした。

　　対流圏観測においては雲の検出・補正が不可欠であり、吸収強度の異なる複数の波長で $O_2\,A$ 帯を観測することで、雲頂高度および視野内雲占有率の２つのパラメータを導出するアルゴリズムを開発した。本アルゴリズムは欧州 ERS-2 衛星に搭載された紫外・可視分光計 GOME の雲補正処理に採用され、高度 65 hPa, 占有率 0.04 の精度で導出されることが実証され、衛星からの対流圏観測の課題を解決した。近年の衛星観測では地球の大半は巻雲かエアロソルにおおわれていることがわかってきており、本アルゴリズムをさらに発展させ、２次元画像化と高光学スループット化により機器の空間分解能を向上させることで、巻雲やエアロソルの高度およびアルビード値を導出する方法を開発した。

　　次に、雲の補正した上で、306-328 nm にある $O_3$ の吸収帯の７つのペアを使い、太陽光の進入高度の波長依存性および吸収断面積の温度依存性を利用して、$O_3$ 全量導出の高精度化、および対流圏成分分離を同時に行うアルゴリズムを示した。放射伝達計算において対流圏 $O_3$ 極大のシナリオを取り入れ、複数の差分吸光値から全量と対流圏成分の同時導出を行うことが本手法の特徴で、複数の観測機器をもちいて全量値から成層圏成分を差し引く従来の方法では不可能であったリアルタイムでの対流圏 $O_3$ の全球観測が実現できる。

　　さらに、紫外連続分光地球アルビード値から消散分光特性を導出し、エアロソルタイプ・粒径・厚さを推定する。$O_3$ の吸収を補正し、$O_2\,A$ 帯で得られた高度情報・$O_2\,A$ 帯近傍でのエアロソルアルビード値を組み合わせることで紫外波長域に吸収をもつ炭素質・鉱物エアロソルを識別する。このようにして可視・赤外の観測では得られない陸域エアロソルの衛星観測が可能になる。

　　最後に、$NO_2$、$SO_2$ などの微量成分をもとめる。以上述べたフローに従い、導出される各物理

量の精度解析をおこない、$O_3$ 全量で 3 DU、対流圏成分に関しては高度分解能 5 km で 10 DU 程度の精度で導出可能であることを示した。このように紫外の連続分光観測と $O_2$ $A$ 帯観測を組み合わせることで、単一の機器で、高度情報を含む大気成分・雲・エアロソルの導出が可能になる。

　次に、開発したアルゴリズムで導出される物理量を観測するための装置の搭載設計・製作・性能評価を行った。全波長域で均一の装置関数を有する Fastie-Ebert 型ポリクロメータを採用し、TOMS の問題点を反映させ、高分光分解能化と低熱歪み構造・光学材料採用による軌道上での波長安定化を実現した。本分光計は入射光学系に 2 つの円柱鏡を採用し、光学スループットを最大化した。さらに、微弱でかつ波長毎に散乱強度の異なる紫外観測において、波長毎に増幅レベルと素子サイズを最適化した大型受光面積を有する C-MOS アレイ素子をカスタム設計した。このような紫外での大気観測用に特化したアレイ検出器の採用は世界初の試みであり、306-452 nm 波長域の高 SNR 観測を実現する。また $O_2$ $A$ 帯用の小型狭帯域フィルタ分光計を入射光学部に設置した。本分光計を用いて天頂散乱光から都市域の汚染 $NO_2$ 気柱量の日変化を観測し、本装置の特徴である高波長安定性と高 SNR を実証した。

　以上のべてきたように、単一機器による大気成分・雲・エアロソルの衛星観測が可能となり、対流圏物理・化学の解明が飛躍的にすすむことが期待される。近年研究が始まった短波長赤外波長域での太陽反射光を用いた $CO_2$, $CH_4$ 全量観測における雲・エアロソルの補正への本アルゴリズムの適用や、フーリエ干渉計を含む短波長赤外・熱赤外波長域の機器開発に関しては付録に示した。まず、成層圏 $O_3$ 化学の解明に不可欠な $ClONO_2$ を太陽掩蔽法で高度分布をもとめるための 0.1 $cm^{-1}$ の分光分解能を有するエシェル分光計の開発について述べた。衛星搭載用として、小型で高い分光分解能を可動部のない回折格子分光器で実現するため、円柱非球面鏡とエシェル型の回折格子を組み合わせた。$ClONO_2$ および微量成分をコンボリューションにより導出するために必須となる装置関数の評価を波長可変レーザで行い、さらに地上で太陽光を取得しその検証をおこなった。次に、高い分光分解能で広波長範囲のスペクトルが得られるために用いられるフーリエ干渉計に関し、太陽掩蔽法観測用に搭載化するため、小型化し、さらに高度分解能を実現するため走査および信号処理の高速化をおこなった。最後に新しい温室効果気体の観測方法として、1.6-1.9 $\mu$m 帯の波長帯を用いたフーリエ干渉計とアルゴリズムを提案した。この波長帯は検出器の冷却が不要であり、主要温室効果気体の吸収帯が限定された波長範囲に存在し、互いの干渉と吸収断面積の温度依存が小さい。散乱反射光は微弱であるが、分解能と観測時定数が最適化すれば十分な SNR が得られることを地上評価により示した。

　21 世紀人類の大気環境の理解と改善のために本論文でのべた機器やアルゴリズムが役立つことを願ってやまない。

# Contents

# Chapter 1 Introduction

**Motivation:** Remote sensing from space is a powerful tool for observing Earth's atmosphere. However, existing instruments provide limited performance. I investigated the physics and chemistry of the Earth's atmosphere from space by using newly developed technology, instrument characterization techniques, and algorithms. In particular, I will propose a rapid algorithm for retrieval of molecules, clouds, and aerosol retrieval in the troposphere with a single instrument using UV and visible continuous spectra data.

## 1.1. Background

There are two methods for observing Earth's atmosphere: *in situ* measurements and remote sensing. *In situ* measurements on the ground can provide accurate data; however, global coverage and vertical profile measurements are difficult. *In situ* measurements by airplane or balloon can also provide vertical profile data, but the observation frequency is limited. Earth observations from the outer space began when the rocket and satellite development commences in the 1950's. Remote sensing from space is a comprehensive method for frequent and long-term monitoring of global changes and for understanding of atmospheric science. Satellite observation has the following advantages over other observation methods.

- Global coverage and frequent re-visiting
- Contributions to data assimilation
- Stable and long-term measurements for monitoring purposes
- Upper troposphere and stratosphere measurements without interference from the ground conditions (limb viewing or occultation)
- Viewing from the top of the atmosphere (nadir viewing).

Development of a satellite and instrumentation entails time and great expense, and there is a risk factor. Therefore, a robust design and multiplepurpose missions are required. In addition, clouds and aerosols must be detected simultaneously for tropospheric measurements and their contamination must be removed. The primary scientific objectives of remote sensing are to monitor the following:

- Atmospheric composition (molecules) (chemical parameters, spectroscopic measurements)
- Radiation budget (clouds, aerosols, upwelling and downwelling flux) (physical parameters, radiometric measurements).

Passive optical methods using ultraviolet (UV) and infra-red (IR) wavelengths are generally reliable for atmospheric molecules composition measurements and provide substantial geophysical information. UV and IR spectra are mainly used because major absorption spectra exist in these regions as indicated in Figure 1-1 and Figure 1-2, and the intensities of an absorption cross section are well known. Only about 10% of the total energy of the input solar flux is UV. However, the UV region is important for understanding heating of the stratosphere and photo-chemical processes, and UV radiation also is harmful to humans. Atmospheric composition measurements generally use the differential absorption method, so spectral fidelity is important. Absolute radiance calibration is required for the radiometric measurement. $O_3$ does not have a fine spectral

1

structure and also must be measured with very accurate UV spectroscopy to meet environment-monitoring requirements. $O_3$ is a dominant absorbing gas and thus can be retrieved independently using a wide spectral range. Minor constituents such as $SO_2$ and $NO_2$ have fine spectral structures and are measured by the spectral-fitting method. Nadir looking measurements are not affected by surface conditions since the Earth surface albedo is low in the UV region. Therefore, UV measurements are suitable for observing global distributions, including land. Furthermore, carbonaceous and dust aerosols have absorption structures in the UV region as shown in Figure 1-3 and spectroscopic measurement of UV can potentially classify the aerosol types. Many atmospheric molecules have absorption spectra that interfere with each other, in the IR region and special techniques, such as the micro window method, are required for data retrieval. These molecules are related to the greenhouse effect and must be monitored with an error level of less than a few percent. Temperature and pressure, which determine absorption intensity, must also be measured simultaneously to minimize the errors.

Wide and continuous spectral coverage, including UV, visible, and IR, is appropriate for radiation budget measurements. These measurements demand superior absolute radiometric accuracy. Both prelaunch and onboard calibration and validation are important for this purpose.
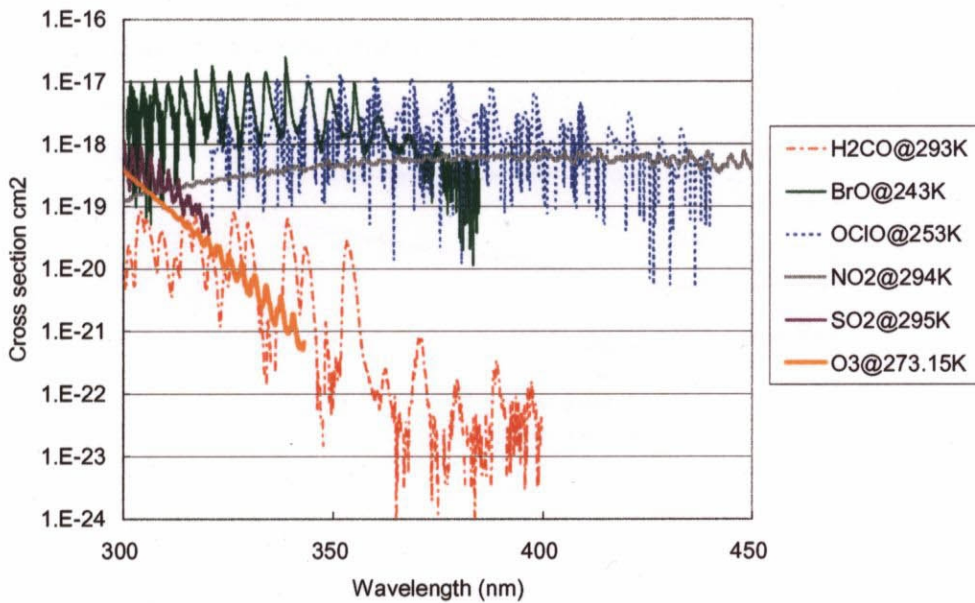


Figure 1-1. Cross section of atmospheric constituents in ultraviolet and visible region.
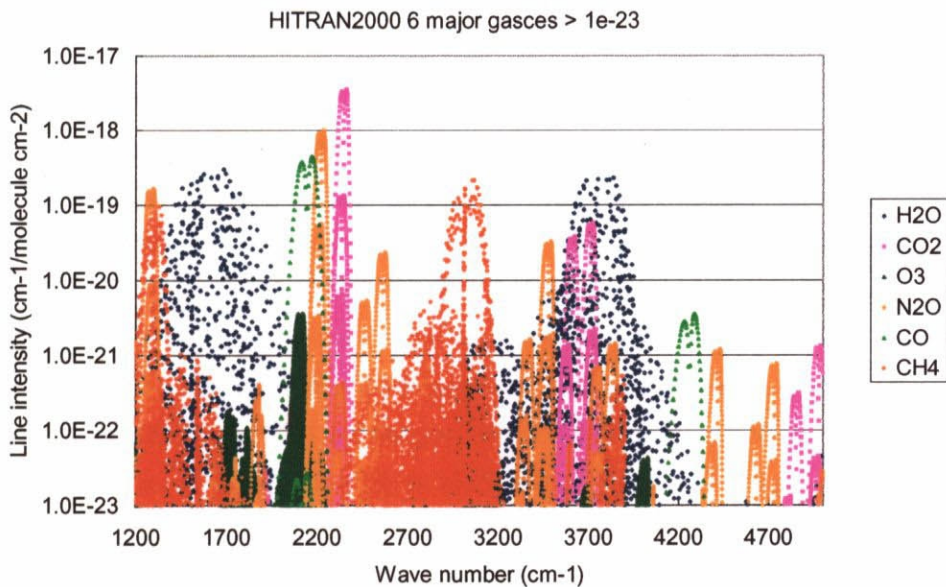
Figure 1-2. Cross section of major atmospheric constituents in infrared region. (Note that wavelength, in nm, is the unit of choice for measurements by the satellite instrument, which are dispersive spectrometers. Line parameter listings are normally in cm$^{-1}$, since line shapes are appropriately described in a scale linear in energy.)
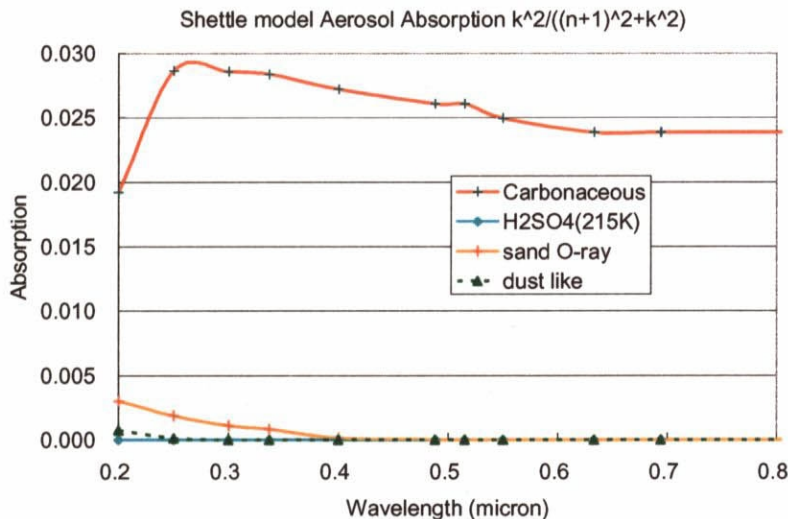


Figure 1-3. Aerosol absorption spectral characteristics in UV and visible region.

## 1.2. Review of Passive Optical Remote Sensing from Space

The history of passive optical remote sensing from space using UV and IR spectral data is reviewed first and is summarized in Table 1-2. One of the most successful programs in the UV region is the Total Ozone Mapping Spectrometer (TOMS), developed by National Aeronautics and Space Administration (NASA) [*Heath et al.,* 1975]. Five models have been launched and four of those have provided the global distribution

3

of total $O_3$ and surface albedo for more than 20 years (NIMBUS from 1978 to 1993, METEOR-3 from 1991 to 1994, Advance Earth Observing Satellite (ADEOS) from 1996 to 1997, and Earth Probes from 1996 to the present). An $O_3$ hole was detected in the polar region, and its expansion has been monitored for over a decade. Sulfur dioxide ($SO_2$) has an absorption band in the same UV region as that of $O_3$ and can be retrieved from the residual of $O_3$ and aerosol absorption. The 14-year NIMBUS 7 TOMS has detected more than 100 volcanic eruptions with sizes greater than 50 K tons of $SO_2$. An $SO_2$ cloud can be traced by daily global measurements with a time constant of about 1 month [*Krueger, 1995*]. Stratospheric Aerosol and Gas Experiment (SAGE)-I, II, and III are solar occultation missions that monitor aerosols, $H_2O$, $NO_2$, $NO_3$, $OClO$, and $O_3$ vertical profiles with a series of instruments (Applications Explorer Mission-2 (AEM-2) in 1979, Earth Radiation Budget Satellite (ERBS) in 1984 and Meteor-3M in 2001). Space shuttle-borne Atmospheric Trace Molecules Observed by Spectroscopy (ATMOS) in 1985, 1992, 1993, and 1994 provided wide IR spectral range data with high resolution; however, the operation time and the latitude covered were limited. The instruments carried on the small science satellites developed by the Institute of Space and Astronautical Science (ISAS) provided the first-generation Japanese atmospheric measurements from space. The EXOS-C satellite carried four instruments for atmospheric measurements: the Backscattered Ultraviolet Spectrometer (BUV), Infrared Limb Absorption Spectrometer (LAS), Aerosol Limb Absorption Imagery (ALA), and Infrared Atmospheric Band Airglow radiometer (IRA) [*K. Suzuki et al.*, 1985]. These first-generation instruments had measured limited types of molecules such as $O_3$. The second-generation instruments were the Interferometric Monitor for Greenhouse gases (IMG) and the Improved Limb Atmospheric Spectrometer (ILAS) borne on ADEOS and ILAS-II on ADEOS-II [*Kobayashi et al.*, 1999, *M. Suzuki et al,.* 1994, 1995]. This generation of instruments provided data of minor constituents and other physical parameters in addition to the major constituents. They also had onboard calibration capability but the performance such as spectral resolution, coverage, and signal-to-noise ratio (SNR), was limited.

The objective of this thesis is to design the advanced third-generation instruments. Several satellite programs to monitor the global atmospheric environment have been planned in the last decade. In 1991, NASA launched the Upper Atmosphere Research Satellite (UARS), which carried Cryogenic Limb Array Etalon Spectrometer (CLAES), Halogen Occultation Experiment (HALOE) and others [*Kramer, 1996*]. NASA is planning to launch EOS-Aura, which will carry the High Resolution Dynamics Limb Sounder (HIRDLS), the Tropospheric Emission Spectrometer (TES), the Ozone Monitoring Instrument (OMI), and Microwave Limb Sounder (MLS). In 1995, the European Space Agency (ESA) launched the European Remote-Sensing Satellite-2 (ERS-2) which carries the Global Ozone Monitoring Experiment (GOME) and in 2002 they launched the Environmental Satellite (ENVISAT), which carries the Scanning Imaging Absorption spectrometer for Atmospheric Chartography (SCIAMACHY), the Michelson Interferometer for Passive Atmospheric Sounding (MIPAS), and others. They also plan to carry nadir looking Japanese FTS on Earth Clouds, Aerosol, and Radiation Explorer (EarthCARE) [*Kimura et al.*, 2002]. The National Space Development Agency of Japan (NASDA) planned to launch the Global Change Observation Mission -A1 (GCOM-A1), which carries Ozone and Pollution Measuring UV Spectrometer (OPUS), the Solar Occultation FTS for Inclined-Orbit Satellite (SOFIS), and the Stratospheric Wind Interferometer for Transport Studies

(SWIFT). These satellite programs will include carry third-generation instruments. Third-generation instruments require stability and fidelity in the form of low thermal distortion and degradation in orbit, in addition to superior spatial and spectral resolution. This thesis primarily describes the instrumentation of a UV polychromator and retrieval algorithm for nadir-looking UV and visible spectroscopy. A retrieval algorithm to correct for clouds and aerosols must also be developed for this purpose.

Table 1-1. History of earth atmosphere observation from space.

| | Satellite program and instruments | Performance |
|---|---|---|
| First Generation | BUV, LAS on EXOS-C | First order geophysical parameters: Total $O_3$, surface albedo, major constituents |
| Second Generation | TOMS, ILAS, IMG on ADEOS ILAS-II on ADEOS-II | Calibration capability Accurate and long term data |
| Third Generation | UV polychromator, Solar occultation FTS Nadir viewing SWIR-FTS | Second order geophysical parameters: Green house gases monitoring with high spatial resolution Cloud and aerosol characteristics |

The geophysical parameters can be retrieved by determining the combination of geophysical parameters in which the difference between the measured spectral radiance or transmittance and simulated value is minimized. Therefore, an atmospheric model that simulates the radiative transfer process (radiation, scattering, and absorption), is important in addition to instrumentation. FASCODE and LBLRTM are widely used radiative transfer models for transmittance and thermal radiation calculations [Clough, 1986, 1992, and 1995]. Several models have been developed and used for UV and visible measurements applications, such as DAVE code, STAR code for TOMS, and LIDORT for GOME and GOME2. These models include multiple scattering effects [Dave, 1964, T. Nakajima, 1988, Spurr, 2001]. In addition, the databases included in the radiative models, such as the molecular line intensity, scattering coefficient and its phase function, solar irradiance, surface albedo, aerosol model, and profile model, are also important for accurate measurements. HITRAN is one of the most frequently used molecular line intensity databases. It has been compiled and updated for more than three decades [Rothman, 1987, 1992, and 1998]. The total $O_3$ retrieval using the STAR code and a spectra comparison between measured data on the ground and simulated data by FASCODE are discussed in this thesis.

Figure 1-4 depicts the geometry of several observation methods for passive Earth atmosphere observation from space. Solar occultation is a method that scans the vertical profile by using the satellite orbit motion. A high SNR and spectral resolution can be achieved simultaneously since the light source is the Sun. However, the total number of observations is limited. Nadir thermal radiation observations measure thermal radiation from the surface, atmosphere, and clouds. The radiance of the light source is weak, and the optics must be carefully designed to minimize the thermal background radiation. Carefully tuned inversion and temperature profile information are needed to retrieve the atmospheric constituent vertical profile, and cloud

5

contamination must be removed. The third method uses an artificial light source, such as a laser on the ground. The laser wavelength must be tunable and the light source should be tracked on board when measuring trace gases. This method is suitable for total column amount, but the observation is limited to where the light source is located. Limb thermal radiation is used to measure the thermal radiation from the atmosphere. A high vertical profile resolution can be achieved without interference from the Earth's surface. The light source is very weak due to the cold temperature of the upper atmosphere, and the instruments are complicated by cooled optics and detector. The limb scattering method is used to measure the scattered light of the Sun. The effective optical path must be corrected since the light path is long and clouds and aerosols can cause interference. The last method is nadir scattered and reflected light observations. An accurate radiative transfer model is necessary to retrieve geophysical parameters since the penetrated solar flux is multiply scattered by the Earth's atmosphere. This thesis primarily discusses nadir-looking scattering observations. The observation methods for solar occultation and limb scattering observations are described in the Appendix.
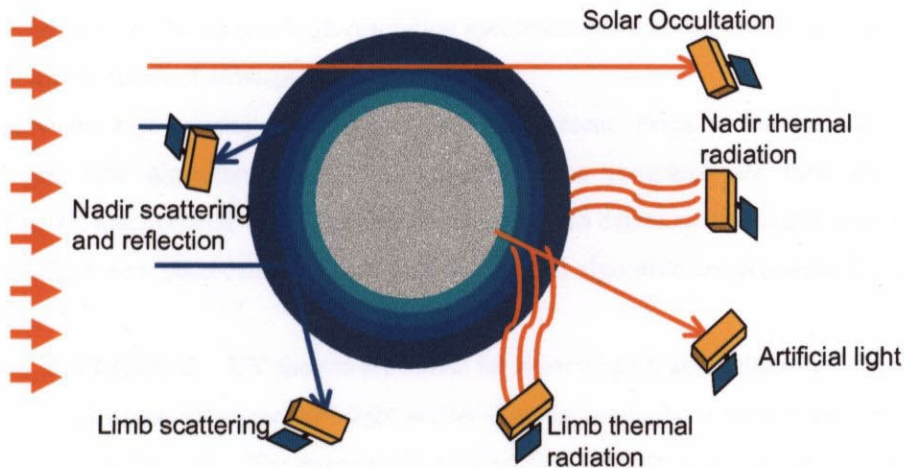


Figure 1-4.  Geometry of the passive earth atmosphere observation from space.

## 1.3.  Environmental Monitoring and Scientific Objectives

The following environmental monitoring issues must be studied [*Ramanathan and Crutzen*, 2001, IPCC Third Assessment Report - Climate Change, 2001, and *Jacob*, 2002].

**Ozone depletion:** Long-term and accurate monitoring of the total $O_3$ are required, and related trace gases must be monitored to clarify $O_3$ chemistry.

**Global warming:** Both long-life ($CO_2$ and $CH_4$) and short-life (aerosol, tropospheric $O_3$) constituents must be monitored.

**Air quality:** Aerosol and oxidization processes.

This thesis discusses the instrumentation and retrieval algorithm to improve the measurement accuracy of the total $O_3$ and depletion from space. The grating spectrometer that measures chlorine nitrate ($ClONO_2$), which is crucial for understanding $O_3$ chemistry, is described in the Appendix. The last two items are

tropospheric measurements that require frequency and removal of cloud contamination. The aerosol must also be considered. Tropospheric $O_3$ is important for both global warming and air quality. $O_3$ is a suitable index of oxidization process, since OH is difficult to observe from space. Another objective of this thesis is to investigate the tropospheric global and frequent observations from space.

## 1.4. Introduction to this Thesis

Minor constituents must be measured for advanced scientific observations, such as those to clarify the $O_3$ depletion mechanism; high spectral resolution is required to achieve sufficient sensitivity and to avoid interference from other constituents. Monitoring from a satellite orbit is suitable for the upper atmosphere, such as the stratosphere and upper troposphere, because data can be retrieved without interference from the surface or clouds. The existing instruments are not properly designed to meet current requirements for monitoring human impact in the troposphere. Improved performance, a new observation method, and a retrieval algorithm are needed to meet these requirements. The instrumentation of a UV spectrometer using a modern detector, optics, and data-processing technologies, and their retrieval algorithm are discussed in this thesis. This study demonstrates the feasibility of spaceborne high-resolution spectrometers that can clarify both stratospheric and tropospheric global distributions of atmospheric compositions.

I review previous and existing instruments first and present items to be improved. Advanced technologies and the new algorithm applied to ongoing space programs are then discussed. The instrumentation of an IR spectrometer with high spectral resolution to detect minor constituents is presented in the Appendix. Finally, a new observation method and its retrieval algorithm are proposed for future mission monitoring missions.

**Introduction to Chapter 2.** UV spectra are useful for observing $O_3$ and polluted air elements, such as $SO_2$ and $NO_2$. A UV spectrometer can measure light scattered by the atmospheric molecules that is absorbed by $O_3$ and other constituents on the path. The amount of constituents is derived in such a way that the deviation of the measured and calculated spectral radiance is minimized. Thus, an accurate radiative transfer calculation and appropriate cloud-contamination removal are required. The total $O_3$ and surface albedo retrieval using an existing space-borne instrument (ADEOS TOMS) and its retrieval results are presented first. These results demonstrate the importance of spectral stability in orbit, characterization of the instrument function, and accurate polarization estimation by Rayleigh scattering. The error source of the measurements, the limited geophysical parameters due to the number of spectral bands, and a method to improve the $O_3$ measurements are discussed.

**Introduction to Chapter 3.** Cloud characteristics such as the cloud-top height and coverage should be detected before retrieving atmospheric molecules to improve tropospheric measurements. Cloud characterization and effective optical path estimation using the $O_2$ *A* and *B* bands are described for a presently operating instrument (ERS-2 GOME). A method to rapidly retrieve the cloud-top height has been applied for GOME, and the validation data verify the high accuracy and precision of this method. A balloon-borne experiment to acquire the $O_2$ *A* band line parameters and solar Fraunhofer spectra is also discussed.

**Introduction to Chapter 4.** The retrieval flows and the expected accuracy of the retrieved geophysical

parameters with a UV spectrometer are presented. The height and reflectivity of thin clouds and aerosols can be retrieved by improving the spatial resolution of $O_2$ $A$ band spectroscopy. The aerosol height information contributes to the classification of the aerosol type. Stratospheric $O_3$ absorbs solar UV radiation, which is harmful to the humans and tropospheric $O_3$ produced by human activities, creates a greenhouse effect. Thus, these should be separately retrieved for environment monitoring. Both the total $O_3$ and tropospheric $O_3$ can be retrieved simultaneously by using seven $O_3$ sensitive and insensitive pairs from continuous spectra. The retrieval method for aerosol type, height, and size information is discussed using UV continuous data, in which land and sea-surface albedo are low, and $O_2$ $A$ band data. Minor constituents such as $NO_2$, $SO_2$, HCHO, BrO, and OClO can be measured by the spectral-fitting technique. Furthermore, global coverage over one day using satellite motion and mechanical scanning with 1.8 degrees of spatial resolution can monitor the dynamics of the stratosphere and air in the troposphere polluted from an urban area.

**Introduction to Chapter 5**. An advanced UV spectrometer that can retrieve clouds, aerosols, tropospheric $O_3$, and polluted air ($SO_2$ and $NO_2$) has been designed by expanding the wavelength region and acquiring continuous spectra. A polychromator technique using a custom 1D array detector with amplifiers and robust optics under the space thermal environment to minimize the moving mechanism and maximize the optical throughput and integration time is described. Scatted UV spectra were acquired with high SNR using the engineering model. This spectrometer includes filter radiometers that use an $O_2$ $A$ band cloud-detection technique. Data of the diurnal variation of polluted $NO_2$ measured by the engineering model is also presented.

**Introduction to Chapter 6 (Appendix)**. There are many absorption lines of green house gases and other trace gases in the IR wavelength region. Fourier transform spectrometers (FTS) are widely used for laboratory and ground IR spectroscopy measurements. However, a long optical path difference, obtained thorough use of a large instrument, is necessary to achieve high spectral resolution. In addition, mechanical scanning requires lengthy observation. These characteristics are not suitable for space-borne measurements. Compact spectrometers with moderate spectral resolution are specifically designed for space-borne measurements. A spectrometer using echelle grating and a combination of rectangular slit and aspherical cylindrical mirrors for the specific target gas ($ClONO_2$), which is a key species for understanding the $O_3$ depletion mechanism in the polar region, is presented.

**Introduction to Chapter 7 (Appendix)**. The instrumentation of a solar occultation Fourier-transform spectrometer for a wide spectral range is discussed. Rapid mechanical scanning, compact optics using double-path technique, and a photovoltaic MCT detector cooled by a pulse tube cooler are applied to solve the problem specific to a spaceborne FTS. The optimum resolution that can be achieved onboard is $0.1$ cm$^{-1}$ due to the limitation of the instrument resources. Therefore, the instrument line shape function must be characterized before launch to observe the fine absorption lines of the molecules. The prelaunch test results are described in both Chapters 6 and 7. The two instruments (grating spectrometer and FTS) described here were specially designed to be compact and lightweight. They are designed to measure the vertical profiles of minor atmospheric constituents. However, those are solar occultation missions in the thermal infrared regions. Therefore, the instruments are still complicated since the Sun-tracking system tracks an area about 1 km from the obit, which is about 3,000 km from the tangent point, and detectors must be cooled or modulated with a

chopper.

**Introduction to Chapter 8 (Appendix).** Special care must be taken with tropospheric measurements to meet the recent requirements for monitoring the source and sink of greenhouse gases from space. Existing spaceborne instruments, such as solar occultation and thermal emission measurement devices, have difficulty retrieving tropospheric constituents. Solar occultation is limited to the upper troposphere due to attenuation of the light and difficulty with immediate Sun-tracking after satellite sunrise in orbit. The horizontal spatial resolution is also limited. Thermal emissions from the nadir require temperature vertical profile information to retrieve atmospheric constituents, and the limb emission measurement requires instrument cooling to detect weak light by minimizing background radiation. The proposed method to monitor greenhouse gases using sun glint over the sea surface and scattered light over land for column density and limb-scattered light for the vertical profile in the short wave infrared region is discussed as a next generation monitoring instrument. The feasibility is verified by presenting the ground data using the laboratory model

Figure 1-5 schematically illustrates the contents and study flow of this thesis. The instruments discussed in this thesis are summarized in Table 1-2.
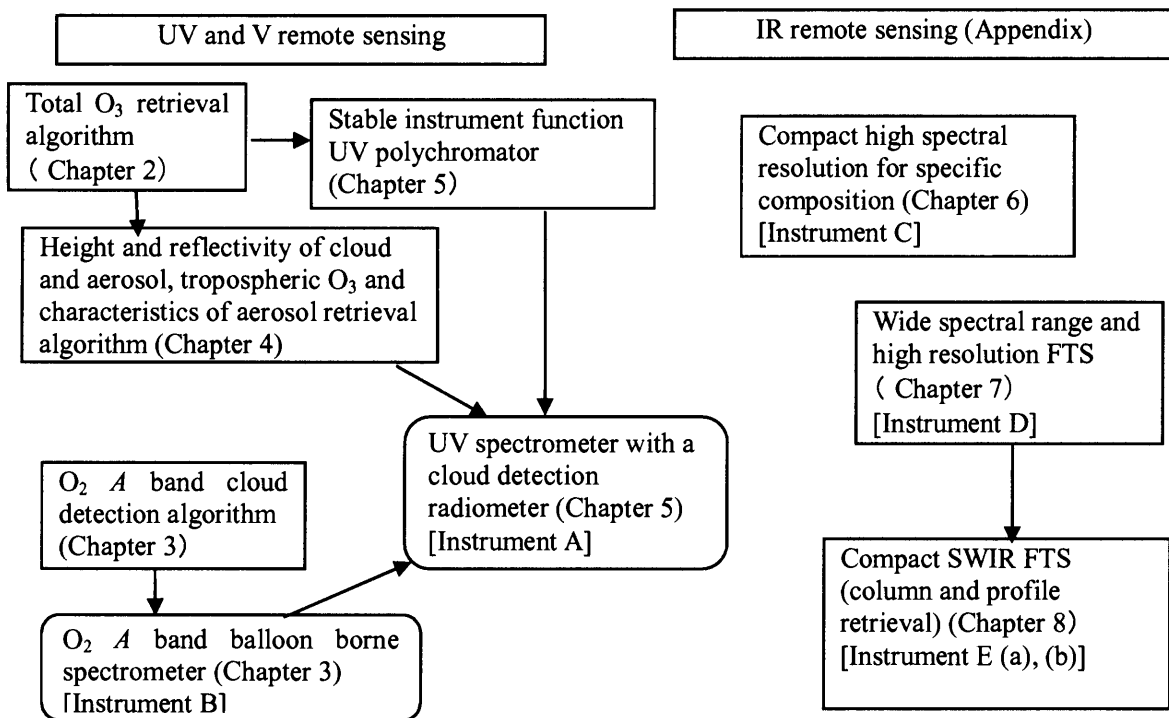


Figure 1-5. Contents and study flow of this thesis.

Table 1-2.  Summary of the instruments discussed in this thesis.

| Instruments | Characteristics | Topics | Acquired data on the ground (ground-based test) |
|---|---|---|---|
| A. UV grating spectrometer | Custom design robust spectrometer | High SNR | Sky light spectra ($O_3$) |
| B. $O_2$-A band grating and filter radiometer | Pressure and temperature retrieval, cloud height | HITRAN and Fraunhofer line data base validation | Direct solar spectra and scattered spectra ($O_2$) |
| C. Solar occultation Echelle grating spectrometer | Compact high spectral resolution (0.1 $cm^{-1}$) FTS | Optical design and characterization of instrument function | Direct solar spectra ($H_2O$, $CO_2$) |
| D. Solar occultation FTS | Compact space borne FTS | Rapid scan for high vertical resolution | Direct solar spectra ($CH_4$) |
| E. SWIR-FTS | (a) vertical profile using spectra | Weak radiance detection | Back scattered spectra ($H_2O$, $CO_2$, $CH_4$) |
| | (b) column amount measurements using sun glint and surface reflected light | Differential absorption measurements with high accuracy | Sun glint over the sea surface and reflected light over land ($H_2O$, $CO_2$, $CH_4$, $O_2$) |

# Chapter 2    Total ozone and surface albedo retrieval with an existing space-borne spectrometer

-Retrieval method by considering instrument function -

The Total Ozone Mapping Spectrometer (TOMS) was launched on ADEOS in August 1996.   It measured total ozone ($O_3$) globally for about nine months.   NASDA EORC developed its own algorithm to retrieve total ozone from the TOMS data using the look-up tables.   TOMS has six spectral channels in the ultraviolet (UV) region to measure solar backscattered radiation.   $O_3$-sensitive and insensitive channels are paired to eliminate the wavelength-independent errors; thus four pairs and one surface albedo channel are employed.   Total $O_3$ is inferred from look-up tables calculated with the radiative transfer on multiple scattering.   The STAR (System for Transfer of Atmospheric Radiation) code used as a forward model.   Surface albedo and total $O_3$ have been retrieved from the level 1 data provided by NASA Goddard Space Flight Center (GSFC).[1]

---

[1] This chapter has been published in "ADEOS TOMS Ozone Retrieval System developed at EORC," *EORC Bulletin* **1998**, 38-54 (1998) and was co-authored by  S. Sasaki, T. Sano and T. Ogawa.   It was updated and revised.

## 2.1. Introduction

Total $O_3$ measurements from satellites are essential for monitoring and understanding the earth's atmosphere. Especially in recent years, frequent and accurate measurements are required for investigating $O_3$ depletion mechanisms. The solar UV is scattered back into outer space and is measured with a space-borne instrument. The penetrated and scattered light is absorbed by tropospheric and stratospheric $O_3$ on the optical path. Thus total $O_3$ is retrieved in terms of UV $O_3$ absorption at Huggins band.

The nadir-look mapping spectrometers on polar orbits can acquire the global total $O_3$ distribution in one day. For two decades, TOMS instruments have been carried on NIMBUS 7 (1978-1993), METEOR 3 (1991-1994), ADEOS (1996-1997) and Earth Probe (1996-). They have six UV spectral channels with 1 nm spectral resolution [*Heath et al.*, 1975]. TOMS onboard ADEOS looks at the nadir with a field of view of 105 deg with 35 steps (IFOV = 44 km on the footprint at nadir) by its mechanical scanner. It has a function to look at the diffuser plate that is illuminated by the sun at sunrise to measure the solar irradiance. Thus the earth albedo is given by the ratio of scattered radiance from the nadir and input solar irradiance. The radiometric response of the instrument and wavelength of each spectral channel are calibrated with the onboard Hg lamps and solar diffusers. The specifications of ADEOS TOMS are the same as the original TOMS except for the spectral channels; the spectral channels of $O_3$ sensitive and insensitive wavelength are replaced with the ones of better $O_3$ retrieval sensitivity than the original TOMS. The ADEOS satellite was launched in August 1996, and was placed in a sun-synchronous polar orbit, whose altitude is 797 km, period is 101 min, recurrent cycle is 41-day and descending local time is 10:41 am with 98.6 degrees inclination. It carried seven earth-observing instruments other than TOMS.

The radiance measured with TOMS is compared with the calculated values for various total $O_3$ amounts and $O_3$ profiles. The total $O_3$ is derived in such a way that the deviation of the measured and calculated radiance is minimized. For the radiance calculation in the UV region, several simulation codes have been developed such as the Dave code [*Dave*, 1964], MODTRAN [*Berk et al.*, 1989], the STAR code [*T. Nakajima et al.*, 1988] and so on. These codes simulate radiative transfer of the earth's atmosphere such as scattering, reflection and absorption by atmospheric constituents. In recent years, with advanced computer technology, radiative transfer codes have improved the quality of $O_3$ retrieval from satellites.

ADEOS TOMS data were acquired at NASA GSFC and the NASDA Earth Observation Center (EOC). Level 1 (raw count data), level 2 (retrieved data of individual orbits) and level 3 (global distribution data) were operationally processed at NASA GSFC. EORC retrieves geophysical parameters such as surface albedo, total $O_3$, and sulfur dioxide ($SO_2$) from the GSFC level 1 data set, to use them for its own researches on developments of data retrieval algorithms and new instruments. The output products at EORC are level 2, level 3 and a global distribution map of total $O_3$ and surface albedo.

## 2.2. Algorithm

### (1) Radiative transfer

The solar UV radiation penetrates into the earth's atmosphere and some part of it is scattered back into

outer space mainly due to the Rayleigh scattering by atmospheric molecules and the Mie scattering by aerosols and cloud particles. In the shorter wavelength range (260-310 nm) the Rayleigh scattering in the stratosphere dominates. The radiation of longer wavelength range (310-380 nm) goes into the lower atmosphere and partially reaches the earth's surface. Therefore, that of longer wavelength is used for measuring total $O_3$ that is the integrated amount of $O_3$ from the surface to the top of the atmosphere. The retrieval of total $O_3$ is based on the differential absorption method. ADEOS TOMS measures backscattered UV at six spectral channels, whose wavelength are 308.68, 312.59, 317.61, 322.40, 331.31 and 360.11 nm according to the post launch calibration [G. Jaross, private communication, 1997]. The $O_3$ sensitive channels (312.59, 317.61, and 322.40 nm) and the insensitive cannel (331.31 nm) are paired. Four pairs are defined as the A-pair (312.59 and 331.31 nm), B-pair (317.61 and 331.31 nm), C-pair (322.40 and 331.31 nm), and D-pair (308.68 and 312.59 nm). The D-pair is used only for the case that the optical thickness is small. Figure 2-1 schematically illustrates the solar UV radiative transfer in the earth's atmosphere. The backscattered solar radiation $I$ is divided into two parts as expressed by equation (2-1): $I_a$ and $I_g$. $I_a$ is the component that does not reach the earth's surface nor cloud top. $I_g$ is the one that reaches the earth's surface or cloud top at least once and reflects back to space, i. e. ,

$$I = I_a + I_g = I_a + FR\frac{T_a}{1 - RT_b}, \qquad (2\text{-}1)$$

where F is the solar radiance, R is the earth's surface albedo (the reflectivity of the ground or cloud top), $T_a$ is the transmittance that the radiation reflected by the earth's surface goes through the atmosphere to outer space, and $T_b$ is the ratio that the reflected radiation is scattered back to the surface. Both $I_a$ and $I_g$ include multiple scattered radiation.

The STAR code is used in calculating multiple scattering in the UV region. The version we use was developed for satellite signal simulation by T. Nakajima [private communication, 1996]. The absorption cross section of $O_3$ is treated as it depends on atmospheric temperature [*Molina et al., 1986; Bass and Paur, 1985*]. $I_a$ and $I_g$ can be calculated with given geometry parameters such as solar zenith angles, view angles from the satellite, and azimuth angles of the sun and satellite and with given values of surface albedo.

13
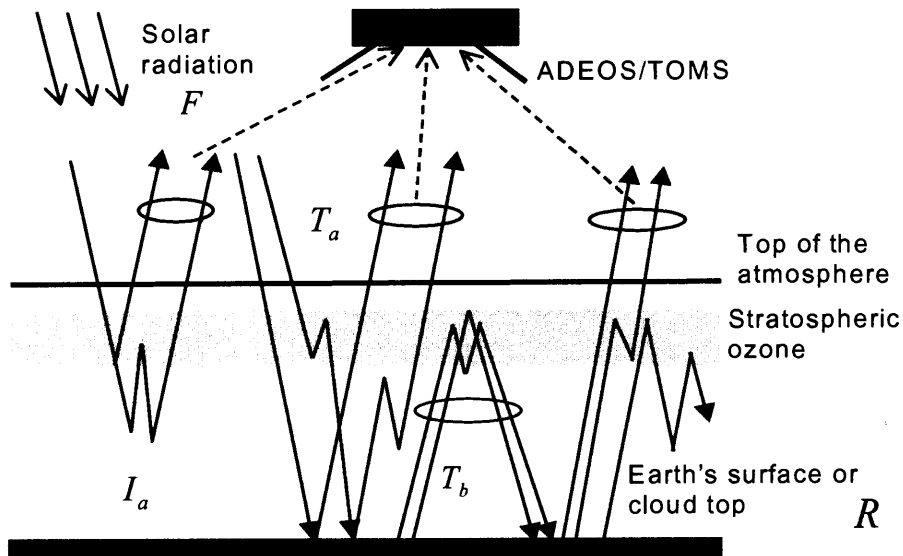
Figure 2-1.    Schematics for radiative transfer in the UV region.


## (2) Retrieval procedure

Figure 2-2 shows the flow of the retrieval process.    The method itself is similar to the TOMS's retrieval algorithm developed at GSFC [*Fleig et al.,* 1990].    As the UV radiative transfer is highly dependent on scattering geometry, the albedo-independent radiance with different geometry is calculated first.    Then the surface albedo is retrieved in each measurement.    Finally comparing the calculated and measured radiance, the total $O_3$ is derived.    The individual processes are described in detail as follows.

Calculate the look-up tables

↓

Receive the measured data set

↓

Calculate the scattered and solar radiance
with the measured data set

↓

Calculate the N-value for a pair

↓

Retrieve surface albedo using the look-up tables

↓

Estimate cloud coverage

↓

Derive the calculated values from the look-up tables

↓

Calculate the radiance adjusted for measured geometry
combining the albedo-dependent and independent parts
with estimated surface albedo and cloud coverage

↓

Interpolate the radiance values
calculated by 50 DU step

↓

Retrieve total ozone

↓

Estimate total sulfur dioxide

Figure 2-2.  Flow of the retrieval for surface albedo and total $O_3$.

## (3) Look-up table

Since the calculation of multiple scattering in the UV region is time consuming, the direct inversion is not realistic.  To reduce the computation time the method using look-up tables is applied in this procedure.  The radiance for a set of parameters is calculated with the STAR code before processing the measured data.  In the satellite data processing, the calculated radiance of the actual measurement geometry is derived by interpolating the values stored in the look-up tables.  As TOMS is not a profile sounding instrument, the $O_3$ altitude distribution must be modeled for the radiance calculation.  Ozone and temperature vertical profiles are modeled as shown in Table 2-1; there are six models for low latitudes, ten models for middle latitudes, and ten models for high latitudes including the case for the $O_3$ hole [A. Krueger and F. Hasebe, private communication, 1996].  The

15

radiance of the each spectral channel is calculated at the center wavelength or 5 wavelength points as listed in Table 2-2. The calculation of the albedo-independent parameters, $I_a$, $T_a$ and $T_b$ in Figure 2-1 are made for the combinations of the following parameters: (1) six spectral channels, (2) cloud at an pressure height of 0.4 atm and cloud-free case, (3) twenty six $O_3$ profiles (different total $O_3$ values by 50 Dobson Units (DU) step at three latitudes), (4) ten solar zenith angles, and (5) six view angles.

Table 2-1. GSFC models for vertical $O_3$ and temperature profile. L, M, and H indicate low, middle and high latitudes, respectively. Ozone and temperature profiles are modeled for every 50 DU of total $O_3$.

Ozone vertical profile (DU)

| Umkehr layer | 0 | 1 | 2 | 3 | 4 | 5 | 6 | 7 | 8 | 9 | >9 |
|---|---|---|---|---|---|---|---|---|---|---|---|
| L225 | 15 | 9 | 5 | 7 | 25 | 62 | 57 | 29 | 11 | 3 | 1 |
| L275 | 15 | 9 | 8 | 12 | 52 | 79 | 57 | 29 | 11 | 3 | 1 |
| L325 | 15 | 9 | 10 | 31 | 71 | 87 | 57 | 29 | 11 | 3 | 1 |
| L375 | 15 | 9 | 21 | 53 | 88 | 87 | 57 | 29 | 11 | 3 | 1 |
| L425 | 15 | 9 | 37 | 81 | 94 | 87 | 57 | 29 | 11 | 3 | 1 |
| L475 | 15 | 9 | 54 | 108 | 100 | 87 | 57 | 29 | 11 | 3 | 1 |
| M125 | 6 | 5 | 4 | 6 | 8 | 32 | 28 | 20 | 11 | 4 | 1 |
| M175 | 8 | 7 | 8 | 12 | 26 | 42 | 34 | 22 | 11 | 4 | 1 |
| M225 | 10 | 9 | 12 | 18 | 44 | 52 | 39 | 25 | 11 | 4 | 1 |
| M275 | 16 | 12 | 15 | 29 | 58 | 64 | 41 | 25 | 11 | 4 | 1 |
| M325 | 16 | 14 | 26 | 45 | 75 | 67 | 42 | 25 | 11 | 4 | 1 |
| M375 | 16 | 16 | 39 | 64 | 86 | 71 | 43 | 25 | 11 | 4 | 1 |
| M425 | 16 | 18 | 54 | 84 | 98 | 72 | 43 | 25 | 11 | 4 | 1 |
| M475 | 16 | 22 | 72 | 108 | 101 | 73 | 43 | 25 | 11 | 4 | 1 |
| M525 | 16 | 26 | 91 | 128 | 108 | 73 | 43 | 25 | 11 | 4 | 1 |
| M575 | 16 | 30 | 110 | 148 | 115 | 73 | 43 | 25 | 11 | 4 | 1 |
| H125 | 10 | 7 | 18 | 8 | 8 | 29 | 22 | 12 | 8 | 3 | 1 |
| H175 | 10 | 8 | 23 | 22 | 27 | 32 | 27 | 15 | 8 | 3 | 1 |
| H225 | 10 | 9 | 28 | 46 | 41 | 35 | 29 | 15 | 8 | 3 | 1 |
| H275 | 14 | 12 | 34 | 67 | 54 | 36 | 29 | 15 | 9 | 3 | 1 |
| H325 | 14 | 15 | 47 | 83 | 65 | 42 | 29 | 17 | 9 | 3 | 1 |
| H375 | 14 | 20 | 61 | 94 | 75 | 46 | 33 | 19 | 9 | 3 | 1 |
| H425 | 14 | 25 | 76 | 105 | 84 | 51 | 36 | 20 | 9 | 3 | 1 |
| H475 | 14 | 32 | 91 | 117 | 93 | 56 | 38 | 21 | 9 | 3 | 1 |
| H525 | 14 | 41 | 107 | 128 | 101 | 60 | 38 | 22 | 9 | 3 | 1 |
| H575 | 14 | 49 | 123 | 142 | 111 | 61 | 39 | 23 | 9 | 3 | 1 |

Temperature vertical profile (Kelvin)

| Umkehr layer | 0 | 1 | 2 | 3 | 4 | 5 | 6 | 7 | 8 | 9 | >9 |
|---|---|---|---|---|---|---|---|---|---|---|---|
| L225 | 283 | 251 | 216 | 201 | 211 | 222 | 231 | 245 | 259 | 267 | 265 |
| L275 | 283 | 251 | 216 | 204 | 212 | 223 | 231 | 245 | 259 | 267 | 265 |
| L325 | 283 | 251 | 217 | 207 | 214 | 223 | 231 | 245 | 259 | 267 | 265 |
| L375 | 283 | 251 | 216 | 210 | 216 | 224 | 231 | 245 | 259 | 267 | 265 |
| L425 | 283 | 251 | 216 | 213 | 217 | 225 | 231 | 245 | 259 | 267 | 265 |
| L475 | 283 | 251 | 216 | 216 | 219 | 225 | 231 | 245 | 259 | 267 | 265 |
| M125 | 237 | 218 | 196 | 191 | 193 | 210 | 228 | 239 | 254 | 264 | 263 |
| M175 | 260 | 228 | 202 | 198 | 202 | 214 | 228 | 239 | 254 | 264 | 263 |
| M225 | 273 | 239 | 213 | 208 | 212 | 219 | 228 | 239 | 254 | 264 | 263 |
| M275 | 273 | 239 | 217 | 212 | 215 | 220 | 228 | 239 | 254 | 264 | 263 |
| M325 | 273 | 239 | 219 | 217 | 217 | 221 | 228 | 239 | 254 | 264 | 263 |
| M375 | 273 | 239 | 220 | 219 | 219 | 222 | 228 | 239 | 254 | 264 | 263 |
| M425 | 273 | 239 | 221 | 221 | 221 | 224 | 228 | 239 | 254 | 264 | 263 |
| M475 | 273 | 239 | 222 | 223 | 223 | 224 | 228 | 239 | 254 | 264 | 263 |
| M525 | 273 | 239 | 222 | 225 | 226 | 226 | 228 | 239 | 254 | 264 | 263 |
| M575 | 273 | 239 | 225 | 227 | 227 | 227 | 228 | 239 | 254 | 264 | 263 |
| H125 | 237 | 218 | 196 | 191 | 193 | 210 | 223 | 237 | 252 | 262 | 266 |
| H175 | 260 | 228 | 202 | 198 | 202 | 214 | 223 | 237 | 252 | 262 | 266 |
| H225 | 260 | 228 | 210 | 209 | 213 | 222 | 228 | 237 | 252 | 262 | 266 |
| H275 | 260 | 228 | 223 | 223 | 224 | 227 | 232 | 237 | 252 | 262 | 266 |
| H325 | 260 | 228 | 223 | 223 | 224 | 227 | 232 | 237 | 252 | 262 | 266 |
| H375 | 260 | 228 | 223 | 223 | 224 | 227 | 232 | 237 | 252 | 262 | 266 |
| H425 | 260 | 228 | 223 | 223 | 224 | 227 | 232 | 237 | 252 | 262 | 266 |
| H475 | 260 | 228 | 223 | 223 | 224 | 227 | 232 | 237 | 252 | 262 | 266 |
| H525 | 260 | 228 | 223 | 223 | 224 | 227 | 232 | 237 | 252 | 262 | 266 |
| H575 | 260 | 228 | 223 | 223 | 224 | 227 | 232 | 237 | 252 | 262 | 266 |

## (4) Wavelength pair

$N_m$-value is defined as the difference of measured backscattered radiance between $O_3$ sensitive and insensitive channels, i.e.,

$$N_m = 100 \times \left( \log\!\left(\frac{L_i}{S_i}\right) - \log\!\left(\frac{L_s}{S_s}\right) \right), \qquad (2\text{-}2)$$

where $L$ and $S$ represent backscattered and solar radiance, and subscripts $i$ and $s$ stand for $O_3$ insensitive and sensitive channels. The pair method can minimize the degradation of the instrument response that is inevitable for space-borne instruments.

$N_c$-value is also defined as the calculated radiance difference between ozone-sensitive and insensitive channels, i. e. ,

$$N_c = 100 \times \left( \log\!\left(\frac{I_i}{F_i}\right) - \log\!\left(\frac{I_s}{F_s}\right) \right). \qquad (2\text{-}3)$$

$I_i$ and $I_s$ can be calculated using equation (2-1).

## (5) Determination of surface albedo

The surface albedo is a variable parameter according to the earth's surface condition and cannot be modeled, but should be estimated in each measurement. The 360 nm channel is used for determining the surface albedo, because it is not absorbed by ozone. Knowing the geometry parameters of the level 1 data set, $I_a$, $T_a$ and $T_b$ values corresponding to the adjacent parameters are derived from the look-up tables and are interpolated to meet the measurement parameters, then the surface albedo R is calculated by solving the equation (2-1).

The clouds play an important role in radiative transfer. So scenarios with and without clouds are prepared. Assuming that the cloud top occurs uniformly at a pressure height of 0.4 atm, the cloud coverage is estimated from the above-calculated R-value as follows; the coverage is set cloud-free for R<0.2, partially cloudy for 0.2<R<0.6 and completely cloudy for 0.6<R. In the partially cloudy case, the coverage ratio within the instantaneous field of view (IFOV) is estimated as the value of (R-0.2)/0.4. This ratio is used as the weight when combining cloud free and cloudy radiance.

Because the surface albedo is calculated in terms of absolute values, it is affected by the instrument degradation on the orbit. A post launch albedo calibration factor is applied for the data processing [G. Jaross, private communication, 1997 and 1998]. ADEOS TOMS shows efficiency degradation, which decreases almost linearly with time. At the end of life, the albedo calibration factor is 1.17 as shown in Figure 2-3.
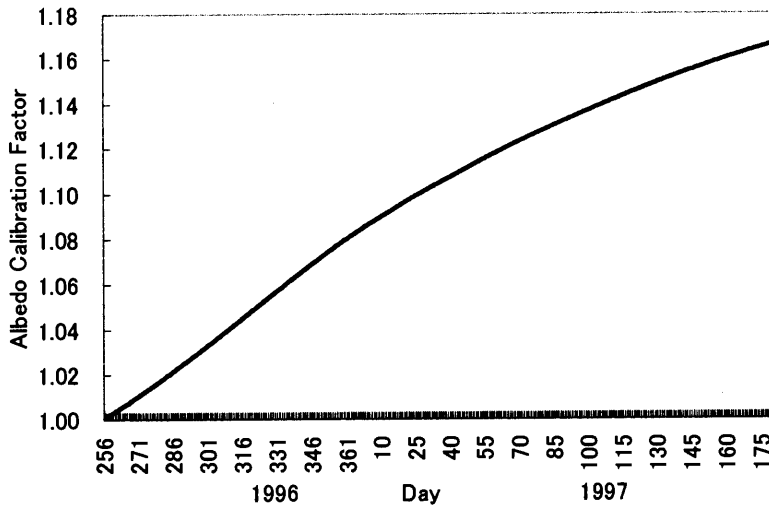
Figure 2-3. Response degradation model (albedo calibration factor) of ADEOS TOMS [G. Jaross, private communication, 1997].

## (6) Determination of total $O_3$

The total $O_3$ is determined by comparing the measured $N_m$-value and calculated $N_c$-value with the 50 DU step of total $O_3$. The best value of ozone is tuned using four retrieved values determined from four pairs (A, B, C, and D). These pairs represent different optical thickness, which is a function of the absorption cross section difference, $O_3$ amount, a solar zenith angle and a view angle. A moderate optical thickness is required for minimum sensitivity to noise, so the C-pair is suitable for optically thick cases, namely high-latitudes measurements where the optical path is large because of large solar zenith angles. The D-pair is suitable for less optically thick cases as seen in low latitudes where solar zenith angles are small and total $O_3$ is relatively small. In the present process we adapt the result from the B-Pair as the best, because the B-pair is suitable for moderate optical thickness and the $O_3$ absorption cross section peak at 317 nm has a plateau structure compared with those of 312 and 322 nm.

## 2.3. Retrieved Results

At EORC the level 2 data set is produced from the GSFC level 1 data set. The orbit information and other parameters such as measured radiance, retrieved $O_3$, and observation time are saved in level 2. Fourteen level 2 data sets taken in one day are combined, interpolated, and saved as level 3. From level 3, a global distribution contour map is created with 128 gradient colors. Examples of the global distributions of the retrieved surface albedo and total $O_3$ are shown in Figure 2-4 and Figure 2-5. The data of 19 September 1996 and 7 March 1997 are chosen. These data were processed with the look-up tables based on the aerosol-free, lambertian-surface and scalar (without polarization) model.

## (1) Retrieved surface albedo

The surface albedo are retrieved globally with 3 degrees view angle step (IFOV = 44 km at nadir). In

Figure 2-4    (a) and (b) the areas of high albedo represent clouds and icy surfaces in the polar region.    As for the look-up tables calculation, the lambertian surface is the default model, there exists differences due to the reflection characteristics.    Especially in high latitudes snow or ice covered areas are specular surfaces, so the error caused by the deviation of the lambertian reflection model increases.



(a)
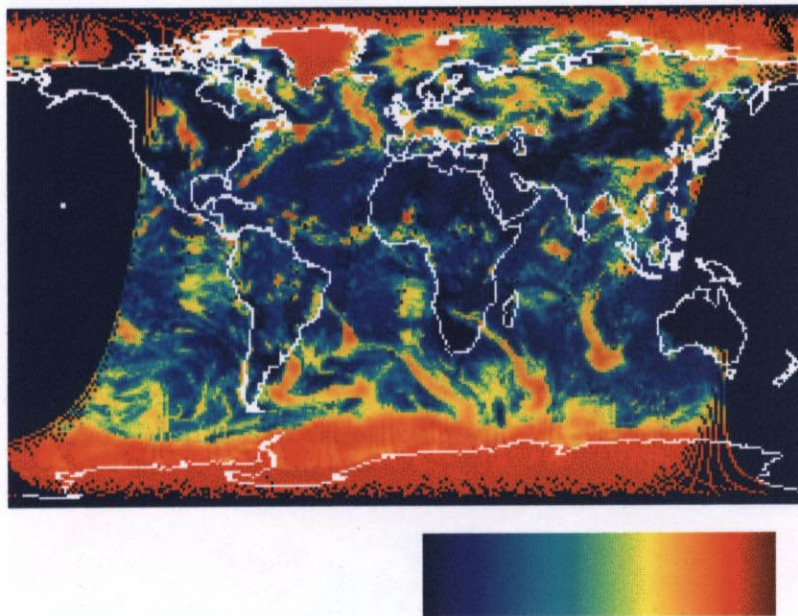
19 September 1996
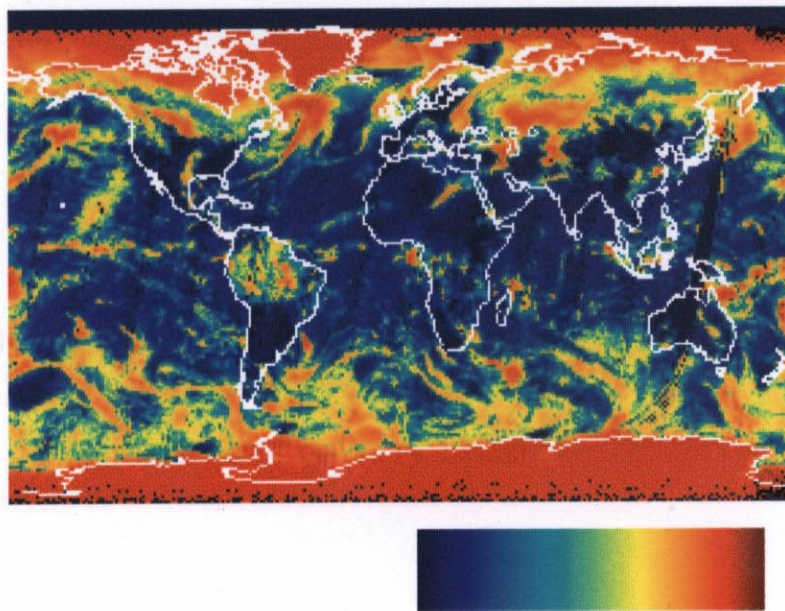


(b)

7 March 1997 (blue 0, red 100%)

Figure 2-4.    Global distribution of surface albedo (a) 19 September 1996 (b) 7 March 1997.    Blue and red indicate 0% and 100%, respectively.

19

(a)
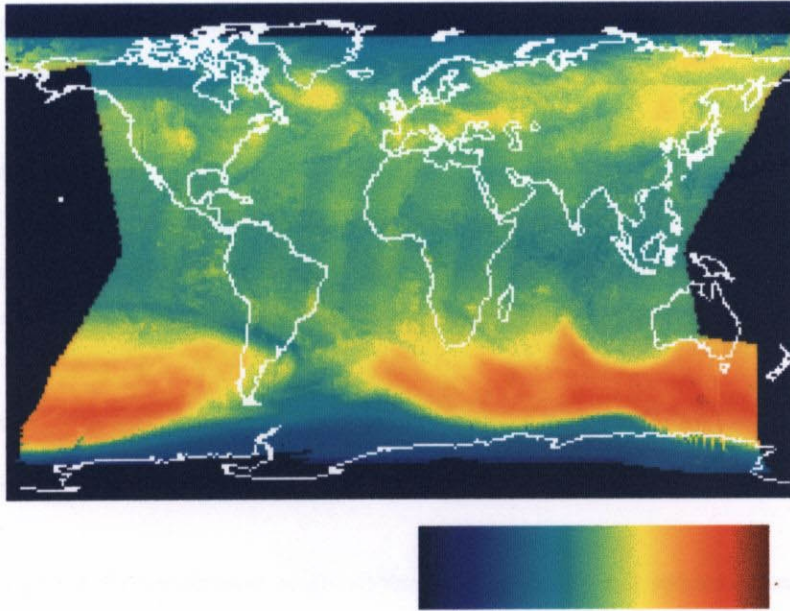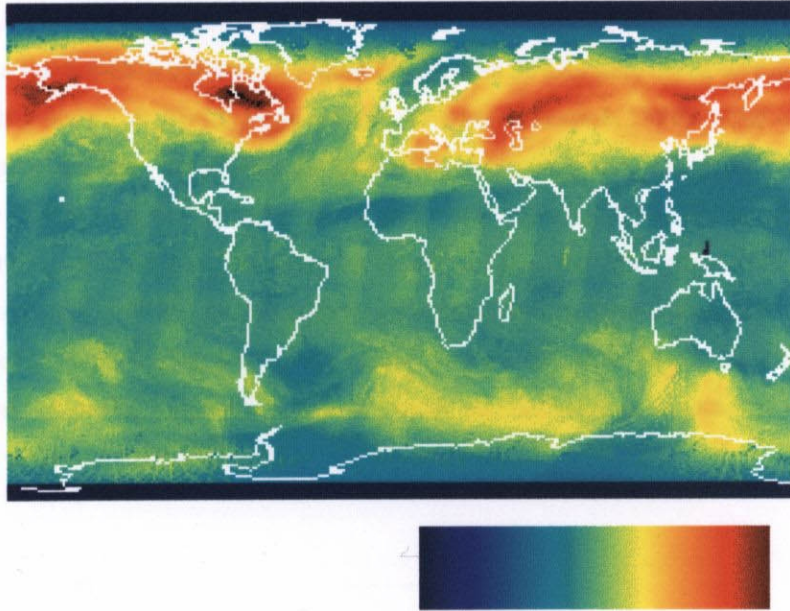
19 September 1996



(b)

7 March 1997 (blue 80, red 500 DU)

Figure 2-5.   Global distribution of total $O_3$ (a) 19 September 1996 (b) 7 March 1997. Blue and red indicate 80 DU and 500 DU, respectively.

## (2) Retrieved total $O_3$

The data of Figure 2-5. (a) was taken during the initial checks of the ADEOS satellite.   Thus it is not a complete global set.   However, it represents the data of the Southern Hemisphere spring, when the Antarctic $O_3$ hole exists.   It also shows the typical $O_3$ distribution features, a large amount of $O_3$ outside the ozone hole, and uniformly distributed ozone in low latitudes.   Figure 2-5. (b) represents the Northern Hemisphere early spring

data and shows the area of low total $O_3$ in the North Polar Region.   From $O_3$ distribution maps, dynamics of the stratosphere can be investigated, too.

### (3) Sulfur dioxide detection

Sulfur dioxide has an absorption band in the same UV region as that of $O_3$, and can be retrieved from the residual of $O_3$ and aerosol absorption [*Kerr et al.*, 1980].   During ADEOS's operation period (September 1996 and June 1997), no huge volcano eruption occurred, so significant amount of sulfur dioxide was not detected.

## 2.4. Discussion

In this section, we will discuss the sensitivity of various factors on the retrieved results.

### (1) Ozone profile

Because the weight of the penetration height differs with geometry and spectral channels, the simulated radiance is sensitive to the $O_3$ profile models.   However the $O_3$ profile must be assumed for the look-up tables calculation.   There is an order of 10 DU difference in retrieved total $O_3$ between assumed profile models, therefore an adequate profile model should be selected according to the latitudes to reduce the retrieval error. Additional profiles for the tropics are shown in Figure 2-6 (a) with 50 DU step, based on the ozonesonde data at Watukosek, Indonesia (Figure 2-6 (b)) [S. Fujiwara, private communication, 1996].   One of the look-up tables is based on these tropical models.   At present the number of ozonesonde datasets is still limited.   To improve understanding of the distribution and variation of $O_3$ and water vapor ($H_2O$) in the tropical troposphere and stratosphere, the Soundings of Ozone and Water in the Equatorial Region/Pacific mission (SOWER/Pacific) has been proposed [*Hasebe, et al.,* 1998].   In this proposal, biweekly sonde observations at three sites, Watukosek Indonesia, San Cristobal in the Galapagos Island, Ecuador, and Christmas Island, Republic of Kiribati, are planned.   Tropospheric $O_3$ profile measurements with sondes and balloons are expected to validate the tropical $O_3$ profile model and to improve the quality of TOMS $O_3$ retrieval.

21
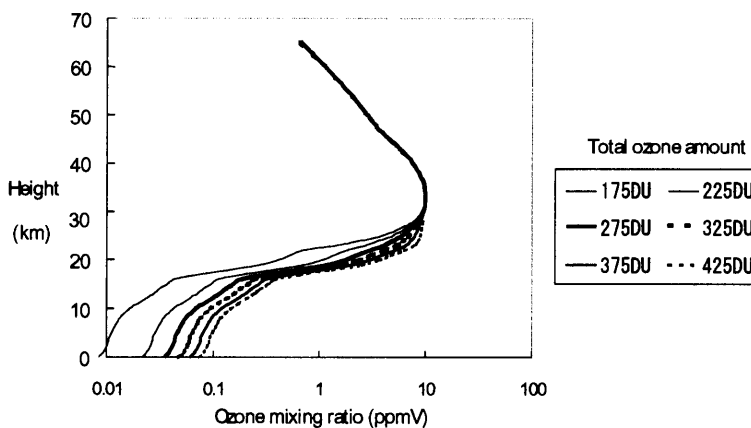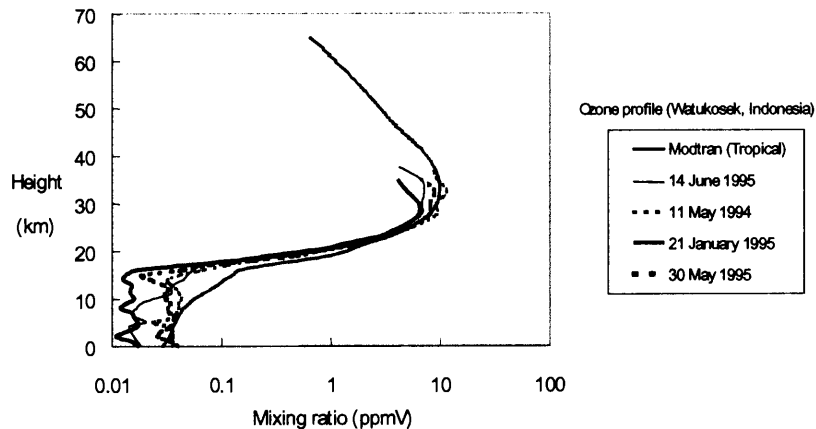
Figure 2-6.   (a) Vertical $O_3$ profile models used for tropics.   (b) Vertical $O_3$ profiles measured with ozonesondes at Watukosek, Indonesia.


## (2) Aerosol

Aerosol is another absorption source of the solar UV.   The STAR code models aerosol concentration as an optical thickness at 500 nm of each layer.   To estimate the sensitivity to aerosol amount, two sets of look-up tables with and without aerosol have been prepared and tested.   Because the aerosol-absorption model has small spectral structure in the UV region, the aerosol effect on the $O_3$ retrieval can be minimized with the differential absorption method.   Due to the limitation of the spectral channels of TOMS, the aerosol information acquired from measured data is limited.   The aerosol effect on the $O_3$ retrieval and aerosol characteristics retrieval using satellite borne polychromator is discussed in Chapter   4.


## (3) Surface reflection

In the calculation of radiative transfer we have assumed the Lambertian surface to the lower boundary, but the Lambertian assumption is not adequate for sea, ice and snow surfaces.   Sun glitter on the ocean surface has been investigated with the STAR code.   The maximum difference in the calculated radiance between a Lambertian surface and the sea surface with 7m/sec wind-velocity at 100m above the ocean is about 15% in long wavelength (360 nm).   These results show the effect on the surface albedo retrieval.   However it is not realistic to prepare look-up tables of several reflection models and select the best one for each measurement.


## (4) Detection of cloud-top height

As the $O_3$ amount below the cloud can not be measured from satellites, it has been modeled assuming that the cloud top occurs at a pressure height of 0.4 atm.   However the actual cloud does not exist at a uniform level of the troposphere and it is difficult to estimate cloud height from the TOMS data itself.   The realistic data on cloud top height deduced from the data from the infrared (IR) imager can be used.   The Ocean Color and Temperature Scanner (OCTS) is also onboard ADEOS viewing the same field with higher spatial resolution than TOMS and it provides a global map of twelve spectral channels from visible to IR.   From IR channels data,

22

cloud height can be estimated assuming the standard temperature profile. The archived OCTS data with the final calibration and validation will be released, and then total $O_3$ retrieved data will be corrected with the $O_3$ amount below the cloud top.

## (5) Polarization

Solar backscattered light by the earth's atmosphere is highly polarized. To simulate the absolute radiance, the polarization effect must be taken into account [*H. Ogawa et al,* 1989]. It is examined by comparing STAR vector (with polarization) and scalar codes (without polarization); the difference depends on the geometry. The maximum difference between the cases with and without polarization is about 10% in the absolute radiance. However the $O_3$ retrieval is relative measurement (differential absorption method) and the polarization effect can be minimized. Because the vector calculation takes about 30 times longer than the scalar one, the look-up tables are calculated with the scalar code to reduce the computation time.

## (6) Wavelength shift and effective center wavelength for radiative transfer calculation

TOMS measures scattered light with 1 nm (FWHM) spectral resolution, which is the convolution of the instrument slit function, the solar Fraunhofer line, and $O_3$ absorption cross section. These factors have a strong spectral dependency and fine spectral structures, thus the wavelength of each spectral channel was updated based on the post launch calibration data. When the wavelength is shifted on board, the look-up tables must be recalculated.

The physical central wavelength is defined as the center of the slit function of the grating spectrometer and it is estimated by NASA GSFC using the onboard data. The effective center wavelength which is defined as the weighted center of the absorption cross section not the same as the center wavelength of the instrument function (slit function), which is the prelaunch calibration data of the instrument. The existing algorithm uses the center wavelength and corrects the retrieved total $O_3$ using the empirical calibration factor. This is because in 1980's computation time is limited and prelaunch calibration for characterizing the instrument function had not been established. In this thesis, the spectral radiance within each spectral channel is calculated at the points listed in Table 2-2. The optical simulation results show the Gaussian like shape instrument function and so weights of the 5 calculation points are 0.07, 0.23, 0.4, 0.23, and 0.07, respectively. By using this method, the convolution of the slit function and absorption cross section are accurately calculated over the wide optical thickness range. Therefore, the viewing angle dependent error, in other words, air mass factor dependent error is removed.

Table 2-2. Wavelength of ADEOS TOMS. [A. Krueger, private communication, 1997] and calculation points of which weights are 0.07, 0.23, 0.4, 0.23, and 0.07, respectively.

| Channel | 1(nm) | 2(nm) | 3 (nm) | 4 (nm) | 5 (nm) | 6 (nm) |
|---|---|---|---|---|---|---|
| Design | 308.60 | 312.50 | 317.50 | 322.30 | 331.20 | 360.00 |
| Prelaunch calibration | 308.84 | 312.76 | 317.74 | 322.53 | 331.44 | 360.47 |
| Post launch validation | 308.68 | 312.59 | 317.61 | 322.40 | 331.31 | 360.11 |
| Radiative transfer | 307.88 | 311.79 | 316.81 | 321.60 | 330.51 | 359.31 |
| calculation points | 308.28 | 312.19 | 317.21 | 322.00 | 330.91 | 359.71 |
| | 308.68 | 312.59 | 317.61 | 322.40 | 331.31 | 360.11 |
| | 309.08 | 312.99 | 318.01 | 322.80 | 331.71 | 360.51 |
| | 309.48 | 313.39 | 318.41 | 323.20 | 332.11 | 360.91 |

## (7) Comparison between pairs

Figure 2-7 illustrates the improvement of the retrieved latitudinal distribution of the total $O_3$ between pairs for scene 17. The result indicates a systematic difference between pairs. The spectral radiance of each channel is calculated at five wavelength points. The D-pair uses the strong $O_3$ absorption, and thus the D-pair value is effective only in low-latitude regions where the total $O_3$ amount and the air-mass factor are small. The retrieved values of the A-pair and C-pair were noisy due to weakness of the signal and absorption. The signal-to-noise ratio (SNR) must be improved to improve the accuracy. However, the systematic error due to an improper effective center-wavelength estimation still remains.
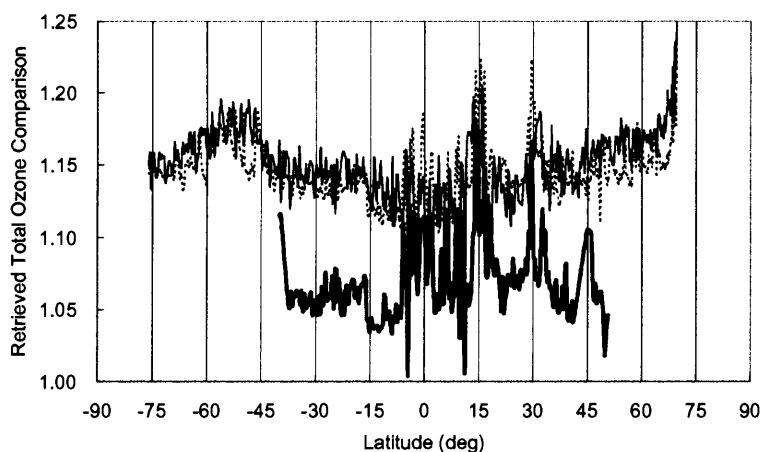


(a)
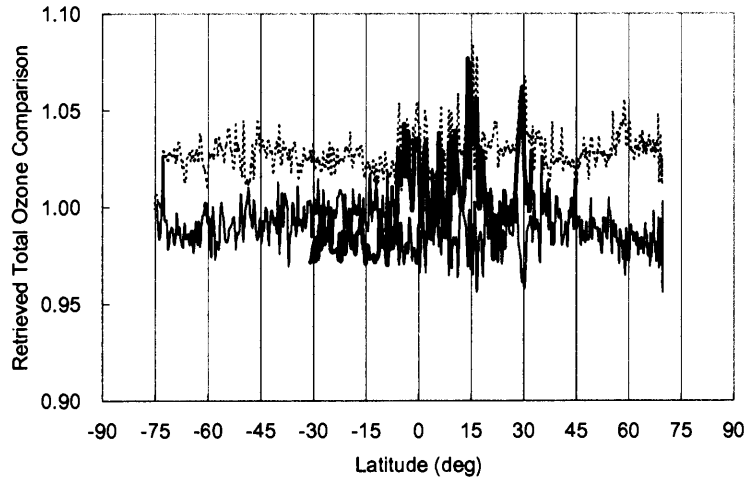
(b)

Figure 2-7. Retrieved total $O_3$ comparison of scene 17 (orbit 471) between pairs of September 19, 1996 (A-pair/B-pair (dotted line), C-pair/B-pair (solid line), and D-pair/B-pair (bold line)): (a) calculated at one point (physical center) per channel and (b) calculated at 5 points per channel.


## (8) Comparison with the retrieved data of NASA GSFC

The total $O_3$ and surface albedo in one orbit has been compared with those processed at NASA GSFC. Figure 2-8 and Figure 2-9 illustrate the difference of the retrieved total $O_3$ and albedo within one orbit from north to south for nadir looking. Figure 2-10 depicts the retrieved surface albedo for side looking. The major algorithm differences between NASDA EORC and NASA GSFC are the empirical correction and radiative transfer models, including the polarization effect. The results indicate that the difference appears in lower-numbered scenes (scene 1 in Figure 2-10) surface albedo, which is the data viewing east with a large scattering angle. The retrieved surface albedo must be corrected since the 90-degree scattering angle has a strong polarization effect. In contrast, the total $O_3$ is retrieved from the differential value of the adjacent spectral channel, and the polarization effect is cancelled.
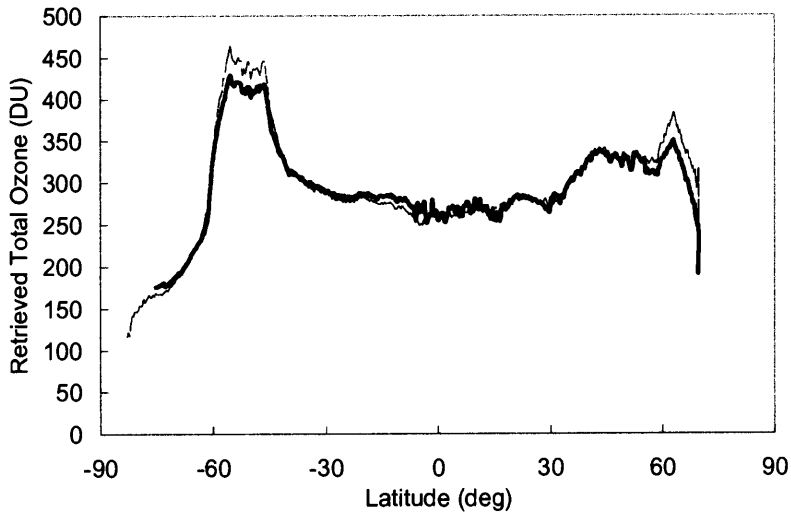
Figure 2-8. Retrieved total $O_3$ (solid line) of 19 September 1996 (orbit number 471) compared with the NASA GSFC (dotted line) level 2 data for nadir looking (scene 17).
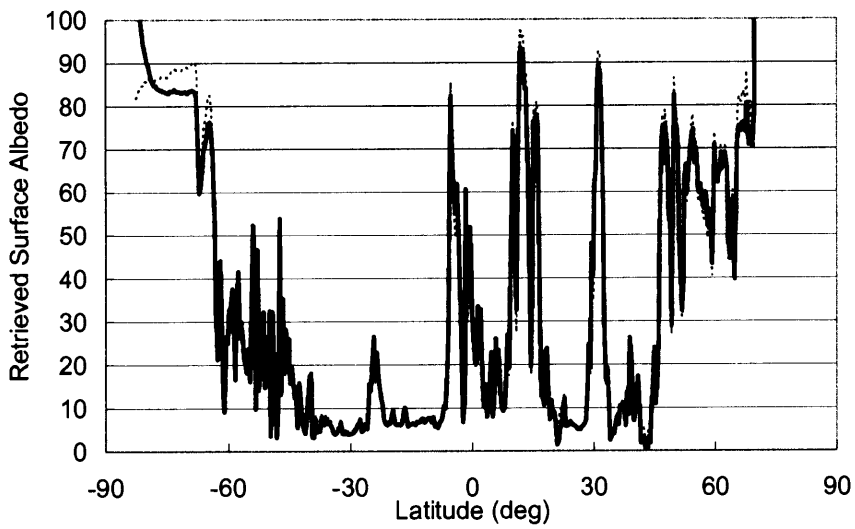


Figure 2-9. Retrieved surface albedo of 19 September 1996 (orbit number 471) compared with the NASA GSFC level 2 data for nadir looking (scene 17).
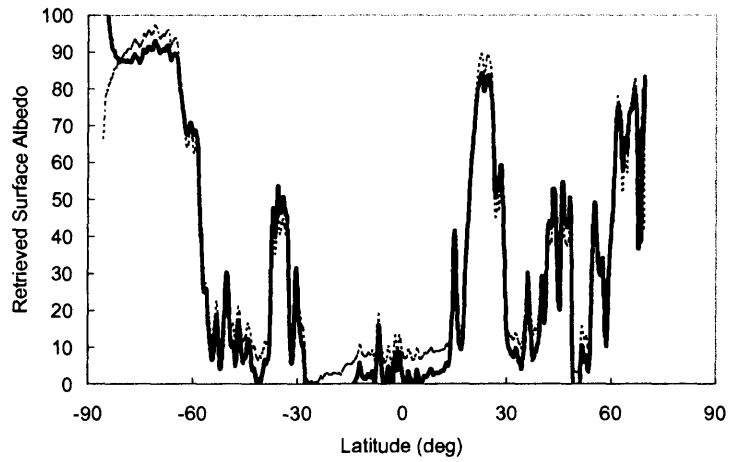
(a)
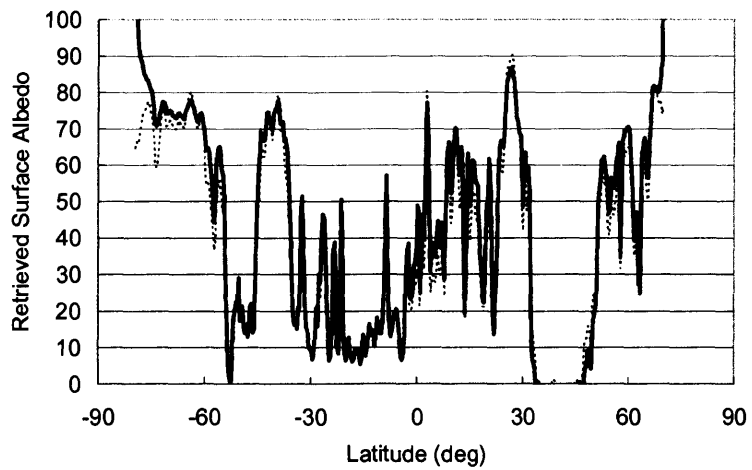


(b)

Figure 2-10. Retrieved surface albedo (solid line) of 19 September 1996 (orbit number 471) compared with the NASA GSFC level 2 data (dotted line) for (a) large scattering angle (scene 1) and (b) back scattering (scene 35).

## (9) Items to be solved and improved for the future mission

By analyzing the TOMS data, the items to be solved and improved for the future mission are extracted. They are summarized in Figure 2-11. The algorithm and instruments improvements will be discussed in detail in Chapter 4 and Chapter 5.

| Not sufficient spectral resolution | Higher spectral resolution (Instrument improvement) |
| Wavelength instability on orbit | |
| | Higher spectral stability (Insrtument improvement) |
| Correction of cloud | |
| Extraction of tropospheric composition | Troposphere measurement (Algorithm and instrument development) |
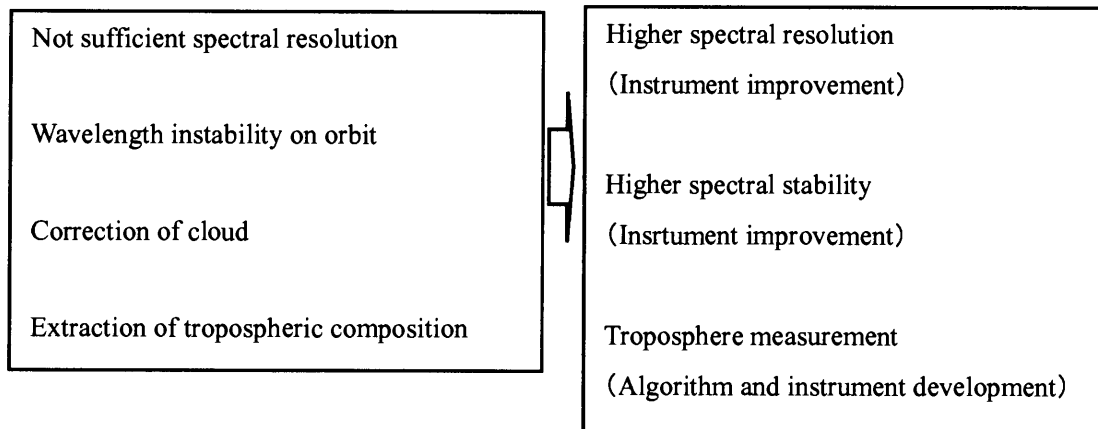
Figure 2-11. Items to be solved and improved for the future mission.


## 2.5. Conclusion of this Chapter

The retrieval system of total zone and surface albedo has been developed and installed at EORC. The system is based on new look-up tables that have been updated when the post launch calibration data of the instrument and $O_3$ profile models were revised. Up to now, ten versions with different calibration constants, aerosol thickness, and $O_3$ vertical profiles are stored in this system at EORC. The best look-up table is tuned by models of $O_3$ vertical profiles, optical thickness of aerosol and so on. The combination of other data sets taken by OCTS and ILAS onboard ADEOS can be applied for the TOMS data analysis. Ground and balloon data with different techniques during the ADEOS validation campaign were also obtained. These combined data analysis will improve the quality of measured data from satellites.

For ADEOS TOMS retrieval, the total $O_3$ had been retrieved by calculating the radiative transfer at the physical center wavelength and multiplying the correction factor since the instrument function had not been measured. However, TOMS channel spectral width is large and the absorption cross section of the $O_3$ varies within a channel and the shape of the instrument function has to be considered. The similar instrument function model has been applied for ADEOS TOMS total $O_3$ retrieval since the slit function of the newly developed laboratory model, which has similar spectrometer to TOMS, has measured and numerically simulated (see chapter 4). The total $O_3$ are consistently retrieved without using the correction factor by calculating the radiative transfer at 5 wavelength points in each channel considering the weight of the instrument function.

TOMS is a sophisticated instrument that supplies trend data for 20 years. This type of UV spectrometers can be improved by replacing the photo-multiplier tube detector to a solid-state array-detector, which gives continuous spectrum information. The UV polychromator is proposed for the next-satellite borne mission, which will cover from 300 to 452 nm spectral region with 0.5 nm spectral and 20 km spatial resolution. The retrieval system for TOMS can be useful for the study on the future instruments and the results also will be reflected in the future instrument specifications and design.

# Chapter 3　Oxygen *A* band spectroscopy and cloud detection algorithm

- Effective optical path estimation method for passive remote sensing -

Cloud height and cloud coverage detection are important for total ozone ($O_3$) retrieval using ultraviolet scattered light.　Use of the $O_2$ *A* and *B* bands, around 761 and 687 nm, by a satellite-borne instrument of moderately high spectral resolution viewing in the nadir makes it possible to detect cloud top height and related parameters, including coverage.　The measured values of a satellite-borne spectrometer are convolutions of the instrument slit function and the atmospheric transmittance between cloud top and satellite.　Studies here determine the optical depth between a satellite orbit and the earth or cloud top height to high accuracy using FASCODE 3.　Cloud parameters are determined by least-squares fitting to calculated radiance ratios in the oxygen bands.　A grid-search method is used to search the parameter space of cloud top height and related parameters to minimize the variance.　For this search, nonlinearity of the atmospheric transmittance (i.e., leverage based on varying amounts of saturation in the absorption) is important for distinguishing between cloud top height and fractional coverage.　Using the above-mentioned method, an operational cloud detection algorithm which uses minimal computation time can be implemented.　Instruments such as those being considered here can measure clouds and atmospheric trace gases in the same instantaneous field of view.[1]

---

[1] The first half of this chapter has been published in "Analysis of cloud top height and cloud coverage from satellites using $O_2$ *A* and *B* bands," *J. Geophys. Res.*, 99, 14481-14491 (1994) and was co-authored by Kelly V. Chance.　The last half is newly added.

# 3.1. Objective

More than 50% of the earth's surface is covered with clouds. Cloud height and cloud coverage detection are important for a number of atmospheric measurement purposes, including total ozone ($O_3$) retrieval and distinction between the stratospheric and tropospheric $O_3$ burdens using ultraviolet scattered light. The NIMBUS 7 TOMS and SBUV instruments use scattered solar ultraviolet light for $O_3$ profile and total $O_3$ retrieval [*Fleig et al.* 1990]. They estimate cloud coverage from measured reflectivity at 340 nm, assuming that the cloud top exists uniformly at a pressure of 0.4 atm. For improvement in environmental monitoring, more detailed cloud detection is required.

To collect enough photons for the required signal-to-noise ratios (SNR) in measurements, a spaceborne spectrometer usually has a larger instantaneous field of view (IFOV) than radiometers like thematic mapper (LandSat-D) and Systeme Probatoire d'Observation de la Terre (SPOT). The large IFOV of the spectrometer will often include both cloud-containing and cloud-free areas. High spatial resolution cloud distribution data is obtained by the spaceborne radiometers, but it is difficult for them to detect cloud height.

Figure 3-1 shows the calculated radiance in the $O_2$ visible region for complete coverage in a few cloud type cases using the radiative transfer model MODTRAN [*Berk et al.*, 1989] in the case of $\theta = 60°$ and $\varphi = 0°$, where $\theta$ is the solar zenith angle (SZA) and $\varphi$ is the nadir viewing angle. The absolute level of the measured radiance depends on the cloud type. Also, it is difficult to distinguish cloud from earth albedo variation. Thus, a method providing direct information on the atmospheric structure, such as the measurement of relative radiances using absorption lines, is necessary for improved cloud parameter detection. Use of the $O_2$ A and B bands, around 761 and 687 nm, is such a method, one which we will demonstrate make it possible to detect cloud height and coverage parameters simultaneously from a nadir-viewing instrument. Cloud altitude estimation using the $O_2$ A band was suggested by *Yamamoto and Wark* [1961], and a detailed study was done by *Wark and Mercer* [1965]. *Saiedy et al.* [1967] determined cloud top height on a GEMINI mission using a spacecraft-borne spectrograph camera with 0.5 nm resolution. *Fischer and Grass* [1991] and *Fischer et al.* [1991] measured the $O_2$ A band with an air-borne 0.6 nm spectral resolution spectrometer having high spatial resolution, and detected cloud top height with 50 m accuracy. However, it is rare that an entire IFOV for a satellite-based spectrometer (typically 100 km × 100 km) is covered evenly by a cloud layer. Therefore, cloud coverage detection is also important. It is shown that, using a moderately high ($\cong 4.0$ cm$^{-1}$ resolution) spectrometer and measuring in several absorption channels, both cloud top height and cloud coverage detection become possible.
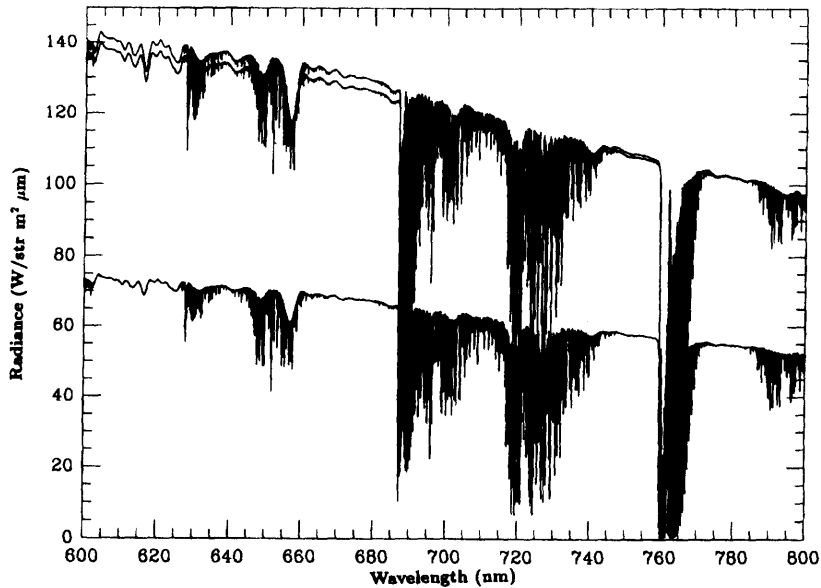
Figure 3-1. Radiance in the visible region for selected cloud types. From the top, altostratus , stratus, and cloud free with surface albedo 0.3.

The study done here is a prototype for the Global Ozone Monitoring Experiment (GOME) and the SCanning Imaging Absorption spectroMeter for Atmospheric CHartographY (SCIAMACHY), which are designed primarily for atmospheric trace gas measurements in the ultraviolet and visible (and, for SCIAMACHY, portions of the infrared). The simultaneous detection of cloud parameters will help considerably in trace gas retrievals. In the ultraviolet and visible regions, incident light at different wavelengths penetrates to almost the same distance inside of clouds; the effective cloud top height doesn't depend strongly on wavelength. Thus, measurements of $O_2$ $A$ and $B$ bands are useful for 300-400 nm cloud top height detection, appropriate to measurements in Hartley and Huggins bands of $O_3$. GOME is a nadir-viewing instrument, while SCIAMACHY includes a nadir-viewing mode. Both have the capability to make measurements at the resolution and accuracy needed for application of the principles investigated in the present study. Thus, both instruments are capable of detecting both cloud top height and cloud coverage with moderate accuracy, when combined with appropriate atmospheric modeling capability. The remainder of this chapter will discuss the cloud detection capability specifically in terms of GOME, but the discussion is equally applicable to SCIAMACHY nadir-viewing measurements.

## 3.2. Radiative Transfer in the $O_2$ Absorption Region

Figure 3-2 shows the $O_2$ $A$ and $B$ spectral bands. $O_2$ $A$ and $B$ have strong absorption around 13143 cm$^{-1}$ (761 nm) and 14546 cm$^{-1}$ (687 nm). (Note that wavelength, in nm, is the unit of choice for measurements by the satellite instrument, which are dispersive spectrometers. Line parameter listings are normally in cm$^{-1}$, since line shapes are appropriately described in a scale linear in energy.) A spectrometer with a spectral resolution of about 4.0 cm$^{-1}$ (e.g., GOME) will have several spectral measurements in the $O_2$ bands. The

31

radiance measured in the satellite geometry by spectral channel $j$, neglecting scattering, is described by:

$$I(j) = \sum_{i=1}^{N} \alpha_{ij} r_i \int f_j(v) F(v) \exp(-s\tau(v, h_i)) \frac{dv}{\Delta v} + \beta_j \left(1 - \sum_{i=1}^{N} r_i\right) \int f_j(v) F(v) \exp(-s\tau(v, 0)) \frac{dv}{\Delta v}, \quad (3-1)$$

where $N$ is the number of different cloud top height types, $\alpha_{ij}$ is the cloud top reflectivity for cloud type $i$ in spectral channel $j$, $r_i$ is the coverage of type $i$ cloud, $f_j(v)$ is the slit function of channel $j$, $F(v)$ is the solar spectrum, $\tau(v, h)$ is the optical depth between cloud top and satellite (proportional to total $O_2$ column amount above the cloud top), $h_i$ is the top height of type $i$ cloud, $\Delta v$ is the full spectral width at half maximum (FWHM) of the instrument and $\beta_j$ is the earth's surface diffusive albedo. $\alpha_{ij}$ and $\beta_j$ are assumed to be constant over the small spectral size of spectrometer channel considered here. It is assumed that clouds are thick enough that solar light reflects at the cloud tops; this is the operational definition of "cloud top" in these studies. The optical path factor $s$ is $\sec(\theta) + \sec(\varphi)$. Radiance in the absence of absorption by $O_2$ or other gases (*e.g.* out of band), without scattering, is described as:

$$I_0(j) = \gamma_j \int F(v) f_j(\gamma) \frac{dv}{\Delta v}, \quad (3-2)$$

where

$$\gamma_j = \sum_{i=1}^{N} \alpha_{ij} r_i + \beta_j \left(1 - \sum_{i=1}^{N} r_i\right).$$

For GOME, $F(v)$ can be measured on-board by the solar diffuser. Thus, the scene-averaged albedo $\gamma_j$ out of band can be directly determined.

Scattering effects are considered below. In the above wavelength region, absorptions by gases other than $O_2$ are small compared with the dominant $O_2$ absorption; they can be safely neglected for cloud detection at the present level of accuracy. $\gamma_j$ in the $O_2$ $A$ and $B$ bands is interpolated using the spectrum near the $O_2$ $A$ and $B$ bands where there is no strong absorption. In this study, the slit function $f_j(\gamma)$ is assumed to be triangular, because the spaceborne spectrometers we are considering have the same output slit (detector) size as the entrance slit. In the real measurements, the slit function must be measured with high spectral resolution. The vertical profiles of $O_2$ number density and temperature are assumed well-known. Optical depths $\tau(v, h)$ between the satellite orbit and each height are calculated with high accuracy using FASCODE 3 [G. P. Anderson and J. H. Chetwynd, private communication, 1992].

The measured values are convolutions of the slit function, $I_0(\gamma)$, and the atmospheric transmittance. It is convenient to describe the convolution in terms of a parameter Q, defined as:

$$Q(j, h_i) = \int f_j(v) F(v) \exp(-s\tau(v, h_i)) \frac{dv}{\Delta v}. \quad (3-3)$$

The parameter $R(v_0, h_i)$, which is the ratio of satellite-measured radiation to solar input radiation, is

then defined by the following, assuming $F(v)$ is constant within a spectrometer channel so that it can be taken outside of the integral in equations (3-1) and (3-2):

$$R(j, h_i, \alpha_{ij} r) = \frac{I(j)}{F(v)}$$

$$= \sum_{i=1}^{N} \alpha_{ij} r_i Q(j, h_i) + \beta_j \left(1 - \sum_{i=1}^{N} r_i \right) Q(j,0) \quad . \qquad (3\text{-}4)$$

$$= \sum_{i=1}^{N} \alpha_{ij} r_i Q(j, h_i) + \left(\gamma_j - \sum_{i=1}^{N} \alpha_{ij} r_i \right) Q(j,0)$$
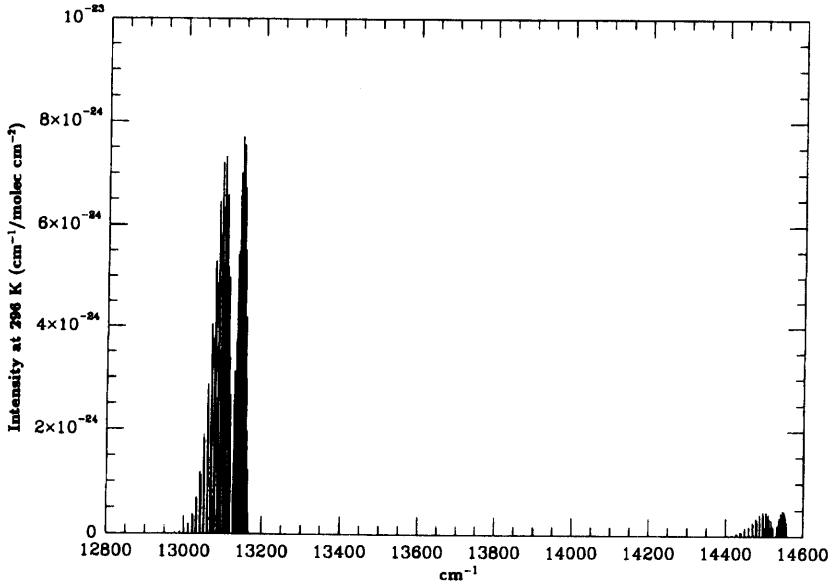


Figure 3-2.   $O_2$ A and B band positions and intensities from the 1992 HITRAN database.

## 3.3.  Determination of Cloud Top Height and Related Parameters

### (1) Grid-search least-squares fit

Cloud parameters are determined by least-squares fitting to calculated radiance ratios.   Assuming there is no *a priori* information on $h_i$, and $\alpha_{ij} r_1$ in equation (3-4), a grid-search method to search the parameter space of $h_i$, $\alpha_{ij} r_1$ to minimize the variance is used.   The quantity $\chi^2$ is defined as

$$\chi^2 = \sum_{j=1}^{M} \left( \frac{R_{obs}(j, h_i, \alpha_{ij} r_i) - R_{calc}(j, h_i, \alpha_{ij} r)}{R_{obs}(j, h_i, \alpha_{ij} r_i)} \right)^2 / M \,, \qquad (3\text{-}5)$$

where the $R_{obs}$ are $R$ values from measurement and ratioing to the measured solar calibration, the $R_{calc}$ are $R$ values for grid searching to determine $h_i$ and $\alpha_i r_i$, and $M$ is the number of spectrometer channels in the $O_2$ $A$ and $B$ band regions ($\alpha_{ji}$ and $\gamma_j$ are assumed to be constant within each $O_2$ band). Here $\chi^2$ is not divided by the error value $\sigma^2$, because $\sigma^2$ is almost the same for each spectrometer

channel. The $\sigma^2$ attained in the measurements determines the contour describing the level of accuracy achieved in cloud parameters, as shown below. The ranges of $r_i$ and $h_i$ are between 0 and 1 and between 0 and 10 km, respectively. Because the ranges are limited, the computation time necessary for searching is not a serious concern. For both cloud top height and cloud coverage detection, optical depth is an important concern. If the optical thickness is too large, it becomes impossible to detect low cloud accurately because the $Q$ values become too small. If the optical depth is too small, the transmittance is an almost linear function of $\alpha_1 r_1$ and optical depth, and it becomes impossible to distinguish cloud height from cloud coverage. If the difference of integrated optical depth between channels is too small it is also impossible to distinguish cloud height from cloud coverage. Thus, for cloud parameter detection, both the optical depth values and contrast between channels are important. Figure 3-3 (a) and (b) show calculated optical depths for a range of typical cloud top height scenarios using FASCODE 3: (a) for $O_2$ $A$ band and (b) for $O_2$ $B$ band. Around this spectral region the GOME resolution is about 4.0 cm$^{-1}$. The optical depths change substantially in this region, so calculations must be done with high spectral resolution. When the spectral resolution is much wider than the oxygen spectral lines in the bands, the measured optical depth is a highly averaged or smeared-out quantity and its variation with detector channel is small. Therefore, higher spectral resolution improves cloud detection. Figure 3-4 shows $Q$ values for several $A$ and $B$ band channels in the case of $\Delta\gamma$ = 4.0 cm$^{-1}$ and $s$ = 2. The center positions of the channels are 13132, 13144, and 14539, and 14551 cm$^{-1}$. Figure 3-5 (a) shows the variation of $\chi^2$ for $\Delta\gamma$ = 4.0 cm$^{-1}$, $N$ = 1, $M$ = 12, $\alpha_1 r_1$ / $\gamma$=0.5, and $h_1$=5 km. The twelve spectrometer channels consist of seven $O_2$ $A$ and five $O_2$ $B$ band measurements. The center positions of the channels are 13132, 13136, 13140, . . . 13156 cm$^{-1}$ for the $O_2$ A band and 14539, 14543, 14547, . . . 14555 cm$^{-1}$ for the $O_2$ $B$ band. N=1 is assumed because there will most often be one cloud type within the IFOV. Figure 3-5 (b) shows the $\chi^2$ variation for higher spectral resolution, $\Delta\gamma$ = 0.2 cm$^{-1}$. The center positions of the channels are 13150.6, 13150.8, 13151.0, . . . 13151.8 cm$^{-1}$ for the $O_2$ $A$ band and 14555.1, 14555.3, 14555.5, . . . 14555.9 cm$^{-1}$ for the $O_2$ band. Figure 3-5 (c) and (d) show cases of lower cloud top heights $h_1$=2 km with $\Delta\gamma$= 4.0 cm$^{-1}$ and $\Delta\gamma$= 0.2 cm$^{-1}$.

Figure 3-5 (c) has several minima, but the proper one is significantly deeper; if the measurement and model accuracy is very good, the solution is unique. For the lower altitude cloud and lower spectral resolution, there are extended trough regions in the variation of $\chi^2$ with cloud height versus cloud coverage. This indicates that high accuracy is required in order to get a unique solution for cloud coverage. Generally, higher resolution is better for cloud detection, but there may be a tradeoff here between resolution and SNR. However, as Figure 3-5 (c) shows, cloud height is easily determined. For total $O_3$ retrieval, the coverage of low cloud may not be critically important. From the hyperbolic shapes of the contours in Figure 3-5 (c), it may be concluded that for low cloud top height and low cloud coverage, the cloud top height is not accurately determined. On the other hand, for the higher cloud top height and higher coverage case, both height and coverage detection accuracy is high.

There is a basic tradeoff in cloud coverage versus cloud height information that stems from the fact that

the most basic accurate information obtained by measurements in the $O_2$ bands, which is that of absorption in the optically thin portions of the bands, gives the average transmission or, equivalently, path length through the atmosphere. Any overestimate of cloud coverage thus implies an underestimate in cloud top height. Figure 3-5 (e) and (f) are moderate and high resolution cases of M = 2, $\alpha_1 r_1 / \gamma = 0.5$ and $h_1 = 5$ km. The resolution is 4.0 cm$^{-1}$ and the center wavelengths of the channels are 13140 and 14547 cm$^{-1}$ for (e); the resolution is 0.2 cm$^{-1}$ and the center wavelengths of the channels are 13151.0 and 14555.5 cm$^{-1}$ for (f). Comparison of Figure 3-5 (e) and (a) shows clearly that the use of a large number of spectral channels greatly improves the accuracy for moderate (*i.e.*, GOME) resolution. However, for higher spectral resolution, a small number of spectral channels is adequate, as shown by Figure 3-5. The above method determines $\alpha_1 r_1$. By using interpolated values of $\gamma_j$, $\beta (1 - r_1)$ may also be determined. If appropriate *a priori* data for $\beta$ is available, $\alpha_1$ and $r_1$ may be determined individually. From the $\alpha_1$ value, it may be possible to estimate the cloud depth. This study is for one cloud type and cloud top height, but the determination of two or more cloud layers within the IFOV is possible with the use of a grid search in more than four dimensions.
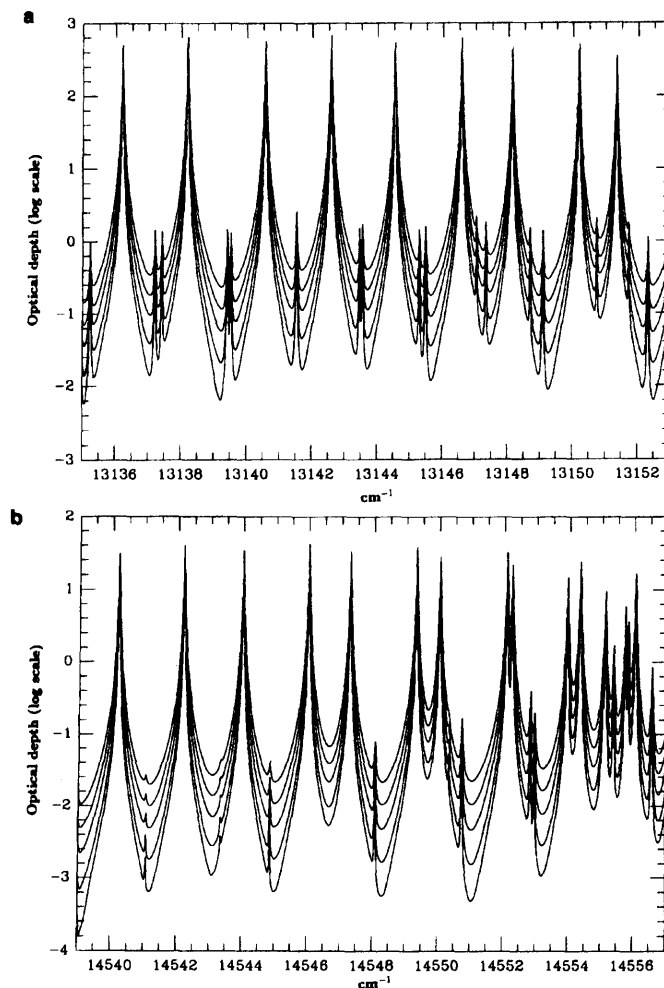


Figure 3-3. Calculated nadir optical depths for the visible band of $O_2$ between space and the altitudes 0 (top), 2, 4, 6, and 8 (bottom) km: (a) $O_2$ *A* band and (b) $O_2$ *B* band.

35
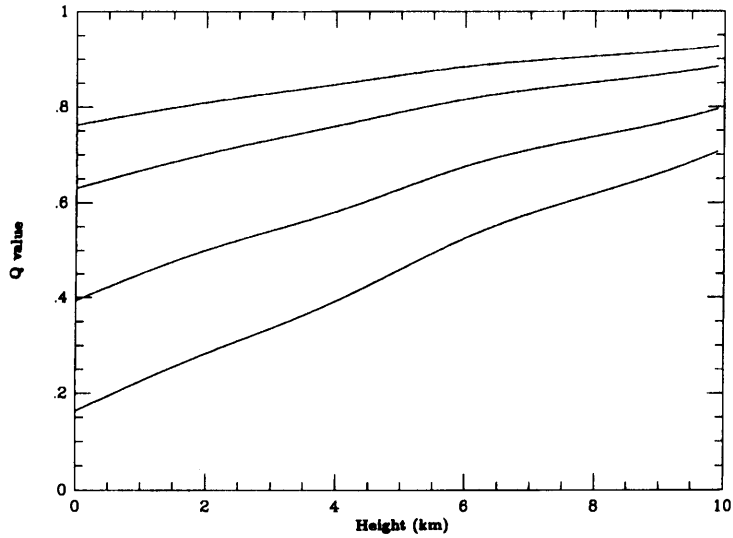
Figure 3-4. $Q$ values (convolutions of the instrument function and the atmospheric transmittance) for $O_2$ $A$ and $B$ band channels with center positions of 14,539, 14,551, 13,132, and 13,144 cm$^{-1}$ (top to bottom) for instrument resolution $\Delta\gamma = 4.0$ cm$^{-1}$.



36
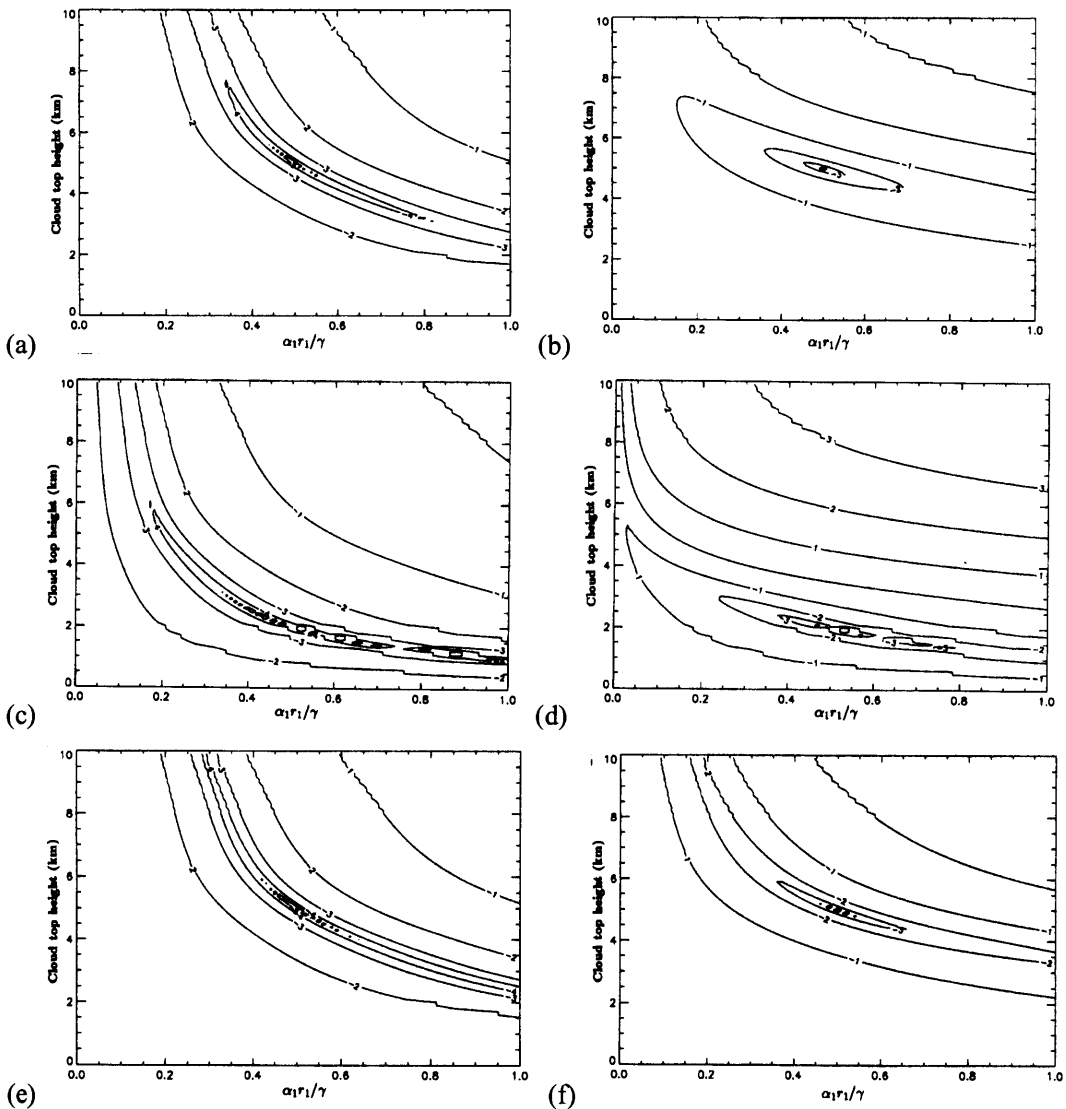
Figure 3-5.  The $\chi^2$ variation in log scale, where $\chi^2$ is the sum of squares of radiance ratio deviations, which is minimized in the fitting process to determine the cloud-top and coverage (see text for details).  Estimated uncertainties are not included in $\chi^2$; rather, the uncertainties determine which contour is applicable.  Results are presented for several case studies illustrating differences due to the number of measurement channels, $M$; the height of the cloud layer $h_1$; instrument resolution, $\Delta\gamma$.  The cloud coverage parameter, $\alpha_1 r_1 / \gamma$ = 0.5, includes a ratio of albedos, as explained in the text.  (a) $M$ = 12, $\alpha_1 r_1 / \gamma$ = 0.5, $h_1$ = 5 km, $\Delta\gamma$ = 4.0 cm$^{-1}$; (b) $M$ = 12, $\alpha_1 r_1 / \gamma$ = 0.5, $h_1$ = 5 km, $\Delta\gamma$ = 0.2 cm$^{-1}$; (c) $M$ = 12, $\alpha_1 r_1 / \gamma$ = 0.5, $h_1$ = 2 km, $\Delta\gamma$ = 4.0 cm$^{-1}$; (d) $M$ = 12, $\alpha_1 r_1 / \gamma$ = 0.5, $h_1$ = 2 km, $\Delta\gamma$ = 0.2 cm$^{-1}$; (e) $M$ = 2, $\alpha_1 r_1 / \gamma$ =0.5, $h_1$ =5 km, $\Delta\gamma$ = 4.0 cm$^{-1}$; (f) $M$ = 2, $\alpha_1 r_1 / \gamma$ = 0.5, $h_1$ = 5 km, $\Delta\gamma$ = 0.2 cm$^{-1}$.

## (2) Accuracy requirements and error estimation

The desired uniqueness of solution determines the accuracy requirement.  As mentioned above, for lower height cloud detection, high accuracy is required.  This statement can be quantified in a typical example.  Figure 3-6 indicates the $\chi^2$ variation for $N$ = 1, $M$ = 12, $\alpha_{ij} r_1 / \gamma$ =0.5, $h_1$ = 5 km, and $\Delta\nu$ = 4.0 cm$^{-1}$.  As before, the twelve spectrometer channels include seven in the $A$ band and five in the $B$ band. The central contour, shown as a bold line, corresponds to the limit of $\pm 1\%$ error about the central minimum. This contour corresponds to $\pm 20\%$ error in cloud coverage and $\pm 2$ km in cloud top height.  If the cloud coverage detection accuracy is required to be $\pm 20\%$, the sum of measurement error and model calculation error must be less than 1%.

The anticipated random errors in measurements are small enough to allow precise solution (the modeled SNR for GOME is $\cong$ 1000), but the forward model calculations in the present study have uncertainties which may cause substantial systematic error.  It is possible to detect the area surrounded by the contour line in Figure 3-6 when the systematic errors are 1%.  This area indicates the correlation between cloud top and cloud coverage and should be useful for removing cloud effects in total $O_3$ determinations.  To separate cloud top height and coverage accurately, higher spectral resolution is required.  The significant systematic error sources are discussed below.  These items are expected to be corrected by adequate calibration.

**Measurement errors.**  Because $R$ is a ratio, that of the earth measurement to the solar measurement, the systematic radiance errors of the instrument response largely cancel.  The capability for relative radiance measurements should be better than 1%.  Model calculation errors include the following items. The first two items affect both $\gamma$ and $Q$ value calculation. The third affects $\gamma$ and the others affect the $Q$ values.

**Single and multiple scattering effects.**  As discussed below, scattering effects must be included for accurate cloud determination.

**Effects of other gases.**  There are strong $H_2O$ bands between the $O_2$ $A$ and $B$ bands, but they don't

affect the $O_2$ $A$ and $B$ bands significantly. In FASCODE 3 studies, we find the calculated optical depth due to other gases within the $O_2$ $A$ and $B$ band limits to be negligible.

**Scene-averaged albedo interpolation in the $O_2$ $A$ and $B$ bands.** The solar spectrum can be assumed to decrease linearly around the $O_2$ $A$ and $B$ bands. The error caused by interpolation is negligibly small.

**Line parameter database.** As discussed below, the line intensities and pressure broadening coefficients must be determined to high accuracy compared to that of the desired detection accuracy, or an appropriate inflight characterization and calibration scheme used.

**Temperature profiles.** According to the *Wark and Mercer* [1965] absorptance calculations, the effect of temperature profile ambiguity on optical depth calculations in these bands (at low spectral resolution) is less than 1%. A calculational check of the temperature dependencies for selected individual line strengths confirms this conclusion for the stronger lines in the A band. The detailed effect of this error on the results of the present method is still under investigation, but we note that 1% measurement error was shown in an example above to cause 20% error in coverage and 2 km error in cloud top height.

**Slit function.** The absolute value of spectral responsivity is not a concern in this method. The shape of the modeled instrument slit function is, however, extremely important.

**Extra absorption inside clouds.** According to Saiedy *et al.* [1967], the estimated cloud top is always below the actual cloud top due to the extra absorption inside clouds. This problem is not serious at the present level of accuracy.
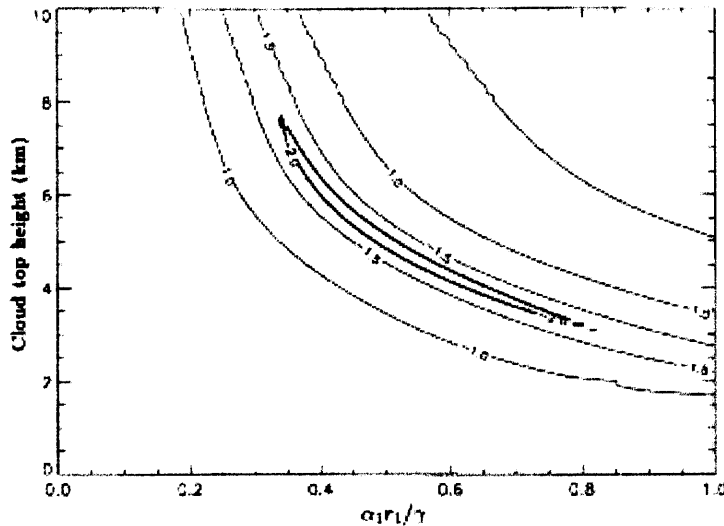


Figure 3-6. The $|\chi|$ variation in log scale; $M$ = 12, $\alpha_1 r_1 / \gamma$ = 0.5, $h_1$ = 5 km , and $\Delta \gamma$ = 4.0 cm$^{-1}$.

## (3) Algorithm and operation

Before launch, the optical depths necessary to determine $Q$ values are calculated for several temperature profile scenarios at a resolution of 0.001 cm$^{-1}$, and the slit function is measured at similarly high resolution. Look-up tables in terms of optical depth are then prepared at intervals of $\approx$ 0.1 km.

After launch, the operational software searches for the minimum $\chi^2$ and estimates the cloud top heights and coverage. The increments for heights and coverages are $\approx$ 0.1 km and 1%, respectively. The default number of different cloud types within the IFOV, $N$, is 1. Thermal differences between ground calibration and orbit, including thermal cycling of the instrument through the satellite orbit, may cause the center wavelengths for the measurement channels to change. Thus, $Q$ values must be re-calculated after the on-board wavelength calibration.

## 3.4. Discussion

### (1) Cloud reflectivity and earth surface albedo

Both $\alpha_1 r_1$ and $\beta(1-r_1)$ are determined in this method. As mentioned above in order to estimate cloud coverage and cloud reflectivity, we will, as our initial working algorithm, employ an *a priori* earth surface albedo table which includes both geographical and seasonal information. The source of the albedo database used to create this table is the ETOPO5 data set (NOAA/National Geophysical Data Center, Boulder, Colorado). More sophisticated future versions of the algorithm should exploit the radiance data from the satellite instrument itself further. GOME and SCIAMACHY each measure the scene-averaged albedo, $\gamma_j$, from 240 nm to 790 nm, including measurements in wide spectral regions where atmospheric gas absorptions are small. As $\beta$ has substantially stronger wavelength dependence than $\alpha_1$, this scene-averaged albedo information should help to further separate surface albedo and cloud coverage. Additionally, cloud scattering studies currently underway at the University of Bremen should provide invaluable information on cloud top reflection coefficients coupled to cloud type and altitude [J. Burrows, R. Spurr, and T. Kurosu, private communication, 1993]. Thus, we anticipate that the proper combination of the satellite radiance measurements and cloud scattering studies will provide the necessary leverage to separate albedo, cloud reflectivity and coverage to high accuracy.

### (2) Scattering effects

Even though Rayleigh scattering is small in the visible $O_2$ absorption region compared with the ultraviolet region covered by GOME, scattering effects must be considered for accurate detection. Single scattering radiance calculations do not depend on either the cloud top reflectivity or earth surface albedo, but when multiple scattering is included there is a strong dependence on both. Therefore, to estimate scattering effects, *a priori* data of $\alpha$ and $\beta$ are necessary. The input radiance $I_s(j)$, including scattering effects is

$$I_s(j) = r_1 \int f_j(v)(\alpha_1 F(v)T(s,v,h_1) + S(v,h_1,\alpha_1))\frac{dv}{\Delta v} + (1-r_1)\int f_j(v)(\beta F(v)T(s,v,0) + S(v,0,\beta))\frac{dv}{\Delta v}, \quad (3\text{-}6)$$

where $T(s,v,h_1)$ is the transmittance and $S(v,h_1,x)$ is the single and multiple scattered radiance.

In general, reflectivity of cloud tops is high in the visible region. Therefore, scattering effects are relatively small and radiance calculation error is small. Out of the $O_2$ absorption region, the scattering affects $\gamma_j$ estimation. The difference between the radiance not considering scattering, $I_0(j)$, and the radiance

39

considering scattering $I_s(j)$ is less than 1% when $\beta = 0.3$, because the back scattering ratio to the zenith is almost equal to the earth surface diffusive reflectivity (note that geometry must be carefully considered when evaluating the importance of Rayleigh scattering in non-GOME geometries, though). A 10% ambiguity of *a priori* $\beta$ in the $s(v,0,\beta(v))$ calculation causes a few percent error in $I_s(j)$. Therefore, the $\gamma_j$ error caused by scattering is less than a few percent. In the $O_2$ absorption region, scattering affects $Q$ value calculations. Because the optical path, including the $O_2$ column density, is multiplied by scattering, the effective optical depth calculation depends on $\alpha$ and $\beta$. For low $\beta$, scattering effects on $Q$ value estimation are relatively high. Therefore, ambiguity in $\beta$ might cause a serious error, and *a priori* data on $\beta$ is important for estimation of scattering effects.

## (3) Spectral band database

The line parameters for these bands necessary to perform the quantitative analysis proposed here are included in the HITRAN and GEISA databases, derived from measurements by *Miller et al.* [1969] and *Giver et al.* [1974]. The line positions are well known for both bands. The intensities for the $O_2$ B band are well known (to better than 2%), but for the $O_2$ A band they are known to only 4%. For both bands, considerable work is necessary on line broadening parameters. Pressure broadening is the chief determinant of line widths, and thus of radiative transfer through the bands, below about 8 km in the Earth's atmosphere.

$O_2$ broadening of the $O_2$ A band lines at room temperature is known to about 15%. No $N_2$ or air broadening studies have been made, and no temperature dependencies have been measured. The values used in the catalogs for $O_2$ A band broadening are actually the more accurately determined $O_2$ B bandwidth parameters (see below), a substitution made on the presumption that the vibrational dependence of pressure broadening coefficients is negligible. Studies for the magnetic dipole-allowed microwave rotationless and far infrared rotational lines [*Chance et al.*, 1991] show that (1) air broadening can be substantially different from $O_2$ broadening; (2) temperature dependence can differ substantially from the suggested hard-sphere value of $T^{-0.5}$; (3) state-to-state dependence, even when sharing a common lower state, can vary substantially between the microwave rotationless and far infrared rotational lines. This fact, plus experience with rotational and vibrational comparisons for other molecules, suggests that the $O_2$ A and B band broadening parameters may differ at a level that is important for detailed geophysical studies. The cumulative error in the widths under atmospheric conditions, considering all of these factors, may well exceed 25%.

The $O_2$ B band intensities and widths are in somewhat better shape, as they were performed at a later time using more fully-developed techniques, but there are still only widths (albeit good to 2-3%) for room-temperature $O_2$ broadening. Broadening values for this band also need to be expanded to include air broadening and low temperatures to be useful for realistic geophysical analysis.

$Q$ value calculations depend directly on line intensities; 2% error in the intensities corresponds to a few percent error in $Q$ value calculation. Although GOME and SCIAMACHY have a $\cong 4.0$ cm$^{-1}$ resolution, wider than the $O_2$ A and B band line widths, the $Q$ values are sensitive to pressure broadening line widths both because the pressure-broadening affects line saturation except in the optically thin limit, and because the slit

function is triangular and the $Q$ values are proportional to convolutions of the line shape and the slit function. The exact sensitivity depends on the line center location in each channel. A 3% error in line width generally corresponds to less than a few percent error in $Q$ value calculation.

Detailed sensitivity analyses to assess the precise effect of line parameter uncertainties on the cloud parameter retrieval accuracy are planned for the next phase of this investigation. This will include more detailed dependence of $Q$ values on line parameters and on the measurement channel placement with respect to the peaks of the $O_2$ lines. Simple radiative transfer considerations imply that the determination of the scene-average path length is a process that depends primarily on the optically thin components of the observations. It is expected that, at the first level of approximation, the knowledge of this quantity depends linearly upon the knowledge of the line intensities. It is also expected that, in order to be able to overcome potentially large systematic effects due to uncertainties in line parameters, an inflight characterization and calibration scheme will need to be devised in order to effectively utilize any data other than optically thin absorption measurements.

## (4) Validation of the cloud retrieval algorithm using the GOME data

*Koelemeijer et al.* [2001 and 2002] applied the cloud-detection algorithm described above to GOME data. They called this algorithm the Fast Retrieval Scheme for Clouds from the Oxygen A Band (FRESCO). They compared it with the thermal infrared imager data acquired with the Along Track Scanning Radiometer-2 (ATSR-2). Data acquired over land (northwest Europe) and the ocean (Atlantic Ocean) were analyzed. The comparison indicated an average difference of cloud fraction estimated to be 0.04 and a standard deviation of 0.09. The average difference for cloud-top pressures was 65 hPa, and the standard deviation was 92 hPa. The results demonstrate that this rapid method provides improved cloud information without using an *a priori* or climatological database. Table 3-1 and Table 3-2 summarize the simulated error level (model calculation) and validated data using onboard measured data as well as the advantages and disadvantages of this method.

Table 3-1. Simulated error level (model calculation) and validated data using onboard measured data.

| Model error (simulation) In the case of systematic error 1% | Validated data using on board measured data by GOME (Koelemeijer *et al.* 2001 and 2002) |
|---|---|
| Correct value<br>cloud top height + 5 km<br>coverage   0.5<br>Error:   height ±2 km<br>coverage ±0.2 | Comparison with the data acquired with ATSR-2<br>Difference           height   65 hPa<br>coverage   0.04<br>Standard deviation   height   92 hPa<br>coverage   0.09 |

Table 3-2. Advantage and problem of this method.

| Advantage of this algorithm | Look up method and grid search method |
| --- | --- |
| | Rapid calculation, easy to tune and minimize the systematic error |
| | Improvement of $O_3$ retrieval |
| | Error decreases by 6-7 DU with information of cloud coverage and cloud top height for cloud height 10 km and coverage 50% (thick cloud) |
| | Simpler than $CO_2$ slicing method (accuracy 1 km) |
| Problem that have to be solved | Detection of thin cloud and aerosol |

## 3.5. $O_2$ Absorption Spectra Measurements with a Balloon-Borne Spectrometer

### (1) Background

The $O_2$ $A$ band is used for pressure and temperature retrieval for the occultation measurements in addition to the cloud-height retrieval. The spectral characteristics of the line intensity have strong temperature dependency, as shown in Figure 3-7. The temperature and pressure vertical profiles can be retrieved by measuring absorption over the entire $O_2$ $A$ band region. ILAS, ILAS-II, SOFIS, and SAGE use this technique [*Sasano et al.* 1999, *M. Suzuki et al.*, 1995, *Kuze et al.*, 2000, and *Pitts et al.*, 1998]. The retrieved temperature and pressure from ILAS onboard data still exhibit systematic difference between sunrise and sunset events [*Sugita et al.*, 2001]. The discrepancy is presumed to be due to thermal distortions in orbit. The ILAS polychromator launched in 1996 has large dispersion and substantial astigmatic aberrations, making the instrument line shape function (ILSF) very sensitive to displacement both on the focal plane and in the defocus direction. The theoretical ILSF was simulated assuming the ideal focus position. However, the actual detector position in orbit may be shifted and the ILSF as built must be characterized using the ILAS engineering model to investigate the instrument status in orbit. In addition, a validated geophysical database for remote sensing application to $O_2$ $A$ band must be acquired. A balloon experiment is planned and the engineering model of ILAS was modified for that purposes. Data with superior spectral resolution and fidelity are expected to be obtained since the light source has high spectral radiance and the spectrometer has sufficiently long enough observation time at the operating altitude.
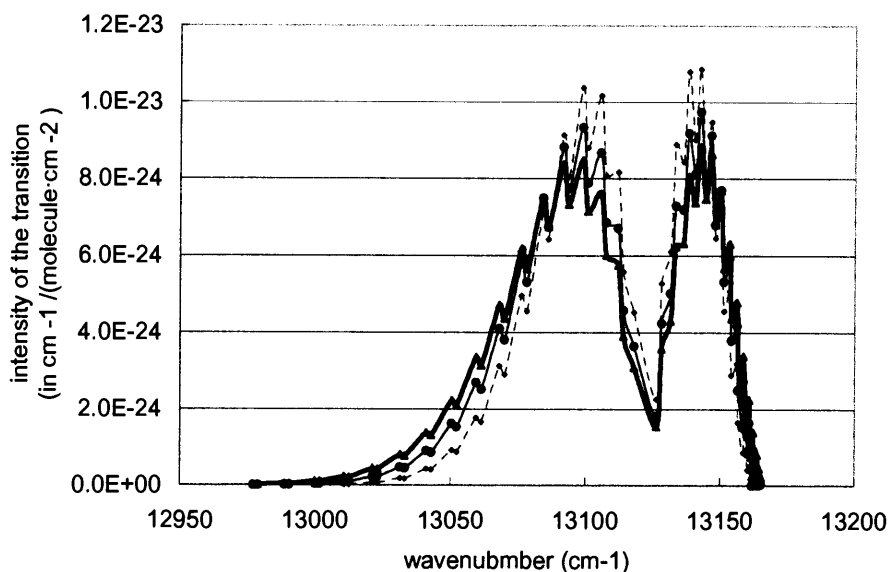
Figure 3-7. Calculated line intensity dependency on temperature. The bold line, solid line, and dotted line represent the intensity of the transition (in $cm^{-1}$/molecule/$cm^{-2}$) of 296K, 250K and 200K, respectively.

## (2) Instrumentation

The engineering model of the ILAS visible spectrometer, which was originally designed and manufactured by Matsushita Communication Industrial Co., Ltd., has been altered by modifying the detector and the entrance slit. The 1024-pixel CMOS array detector was replaced with a 5000-pixel CCD detector. Reducing the pixel pitch and slit width yielded a spectral resolution of the upgraded spectrometer three times greater than the ILAS spectrometer on board. Thus, spectra with a 0.0085 nm interval can be acquired. The detector focus must be carefully aligned at the optimal focus in terms of spectral resolution since the polychromator has a substantial astigmatic aberration. The height of the entrance slit was maximized without degrading the spectral resolution and the actual size is 20 by $340\mu m$. The instrument parameters are summarized in Table 3-3.

Table 3-3. Instrument parameters of modified ILAS $O_2$ $A$ band spectrometer.

| Spectral range | 748-790 nm | |
|---|---|---|
| Optics | Type | Grating polychromator |
| | Grating | 1803 grooves/mm (concave grating) |
| | Slit | 24 by 356 μm |
| Dispersion | 0.0085 nm/pixel | |
| Detector | 5000-pixel CCD (pitch 7 μm) | |
| | Integration time: 65.534 msec | |

## (3) Line parameters

There was still a 10% error in the intensities and line widths. The accuracy of the $O_2$ line parameters must be improved. NASA funded the preparation of a new database using the laboratory measurements [*Pitts et al.*, 1998]. The line parameters of the isotope database also must be also validated since $O_2$ is abundant and the absorption of the second-most abundant isotope is substantial. The spectrometer for a balloon-borne instrument is designed to measure individual spectral lines of $O_2$.

## (4) Fraunhofer spectra

Solar Fraunhofer spectra data measured on the ground with high spectral resolution is available. Kurucz's database of the solar irradiance has very high spectral resolution and is widely used for remote sensing [*Kurucz, 1995*]. However, it is based on a ground measurement and contaminated by Earth's atmosphere. The balloon measurement will provide the high-resolution irradiance data in the upper atmosphere.

## (5) Aerosol extinction and $O_3$ Wulf band

The major error sources in the pressure and temperature retrieval are aerosol extinction and absorption in $O_3$ Wulf band. These data can be acquired as the balloon ascends.

## (6) Performance of the spectrometer

Figure 3-8 depicts the measured $O_2$ absorption spectra in Yokohama, Japan, 3 March on 2002 compared with data from the Bomem DA8 FTS. Figure 3-9 indicates the line position and intensity of most abundant isotope of $O_2$ (square) and second-most abundant isotope of $O_2$ (triangle). The spectra in Figure 3-8 demonstrate that the modified grating spectrometer has sufficient sensitivity and spectral resolution to observe the weak absorption spectra of the $O_2$ second-most abundant isotope. In contrast, the ILAS flight model has insufficient spectral resolution to measure the absorption of the second-most abundant isotope of $O_2$.



44
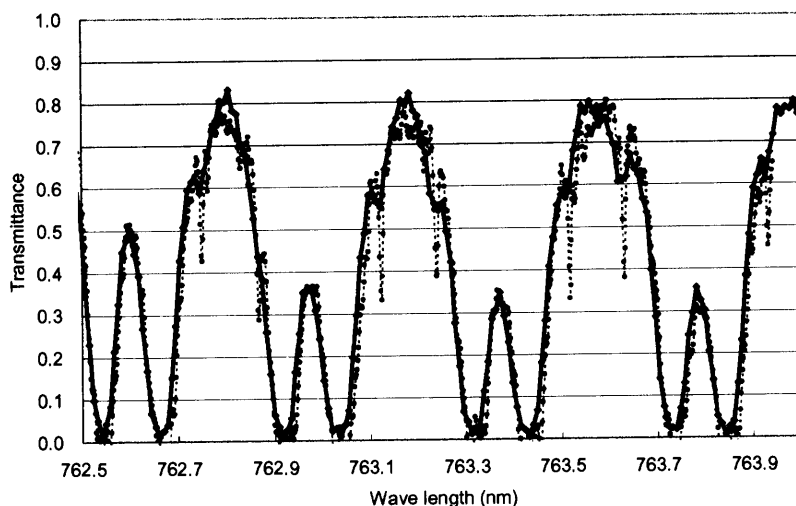
Figure 3-8.   Measured $O_2$ absorption spectra in Yokohama, Japan, 9 March 2002 (bold curve) compared with data with Bomem DA8 FTS (solid curve).   The sampling interval of ILAS EM grating spectrometer and DA8 FTS are 0.148 $cm^{-1}$ (0.00856 nm) and 0.03 $cm^{-1}$, respectively.   The small valley structure shows the absorption of the second most abundant isotope of $O_2$.
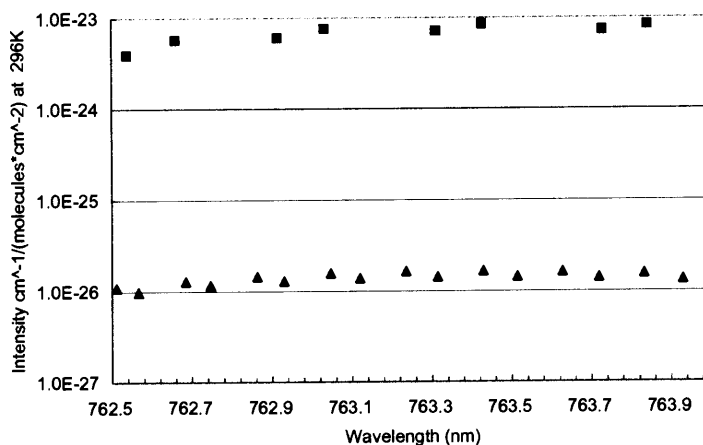


Figure 3-9.   Line intensity of most abundant isotope of $O_2$ (square), and second most abundant isotope of $O_2$ (triangle).

# (7) Optimum spectral resolution

The grating spectrometer discussed here has the same order of spectral resolution as the high-resolution FTS of BOMEM DA8 and is sensitive to environmental conditions.   The data must be accurate and robust since $O_2$ $A$ band absorption is used for optical path length correction.   However, the only information required for solar occultation applications is temperature and pressure.   Thus, a moderate spectral resolution can achieve great accuracy.   Figure 3-10 illustrates the simulated sensitivity to a shift or distortion in orbit, assuming the spectrometer has a Gaussian shaped ILS.   Two cases are simulated: the 4 $cm^{-1}$ resolution of the level of GOME and SCIAMACHY resolution, and the 10 $cm^{-1}$ resolution, which is close to the spectral resolution of SAGE.   The result demonstrates that a spectrometer with greater than 4 $cm^{-1}$ resolution is sensitive to the shift while a spectrometer with a 10 $cm^{-1}$ resolution is insensitive to the shift and is therefore robust.

45

**O2-A band Sensitivity Study ILSF (HMFW=4cm-1)**

(a)

**O2-A band Sensitivity Study ILSF (HMFW=4cm-1)**

(b)

**O2-A band Sensitivity Study ILSF (HMFW=10cm-1)**

(c)
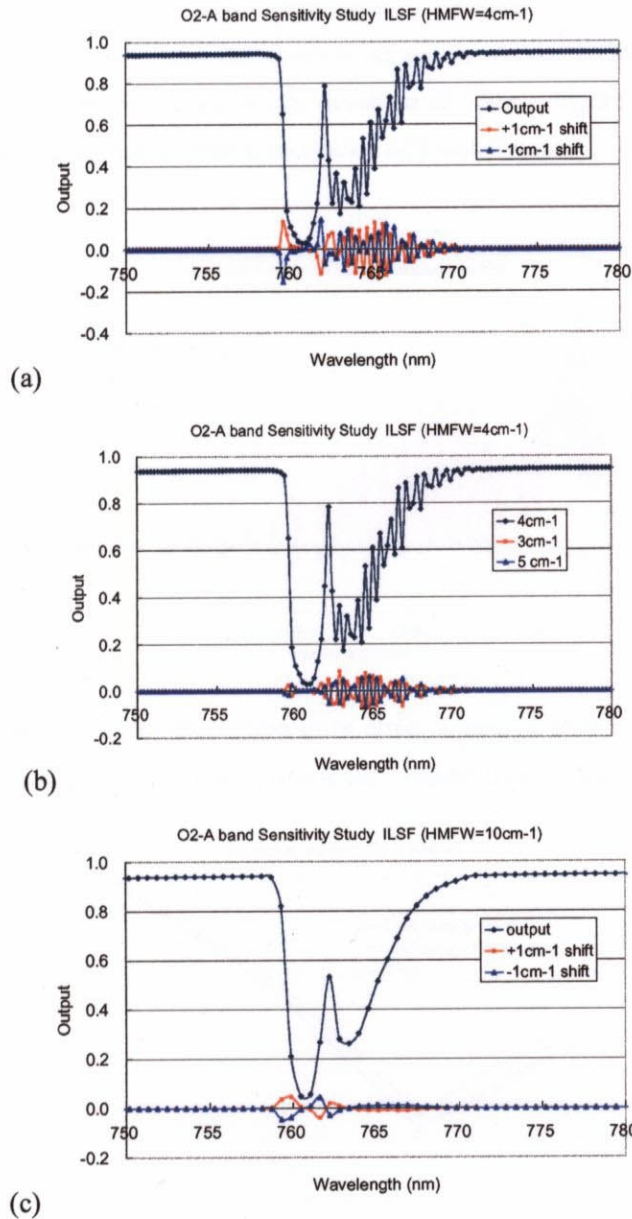
Figure 3-10. Simulated sampled absorption spectra and sensitivity to a shift in orbit (simulated error): (a) +/- 1 cm$^{-1}$ shift (about 50 $\mu$m shift of the detector) in the dispersion direction on the focal plane for a 4 cm$^{-1}$ spectral resolution, (b) shift in the defocus direction for a 4 cm$^{-1}$ spectral resolution, which results in the spectral resolution degradation, and (c) +/- 1 cm$^{-1}$ shift in the dispersion direction on the focal plane for a 10 cm$^{-1}$ spectral resolution.

## (8) Error analysis

A temperature insensitive line should ideally be selected. However, very high spectral resolution is required. A spectral band-pass filter of about 60 cm$^{-1}$ is discussed here instead. The sensitivity to temperature is studied assuming that the typical temperature profile uncertainty level is 10K. The averaged

absorption spectra have relatively low temperature dependency since positive and negative temperature-dependent spectra exist within the spectral region, as shown in Figure 3-11. The temperature dependency is much smaller than the surface height deviation of 1 km. Figure 3-12 depicts the sensitivity to the temperature and surface height for a spectral resolution of 2 and 100 cm$^{-1}$.

O2-A band Transition simulation by FASCODE3P USS 1  Temperature Error Effect
10K error for all altitudes  0.4 cm-1 resolution AMF=2
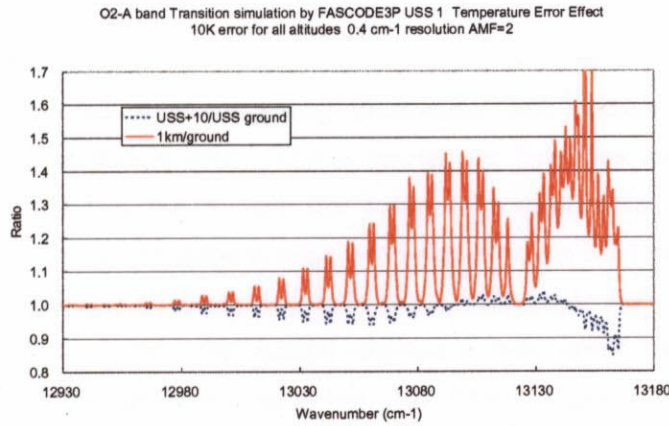


Figure 3-11.   Sensitivity to the temperature error compared with the sensitivity to the surface height for a spectral resolution of 0.4 cm$^{-1}$ and air-mass factor of 2.

Sensitivity study of O2 A AMF=2
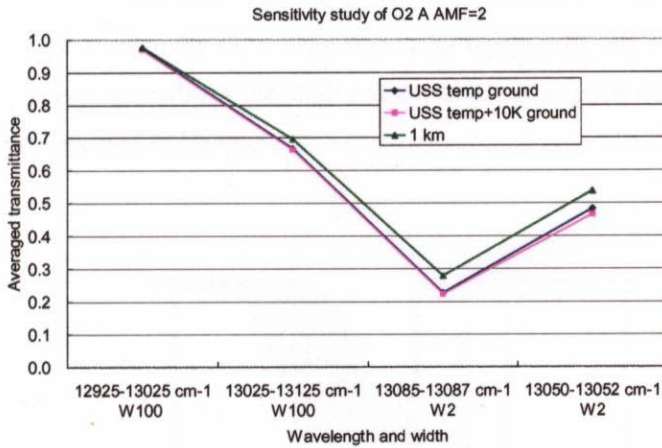


Figure 3-12.   Sensitivity to the temperature error and surface height of $O_2$ $A$ band spectral channel.

## 3.6.   Proposed Nadir-Viewing Instrument for Cloud-Height Detection

### (1)  Trade-offs

The trade-offs among the spectral resolution, systematic uncertainties, and SNR, must be studied.   The geophysical parameters to be retrieved are cloud interference, aerosol extinction, and the vertical profile of temperature and pressure, assuming the line parameters of $O_2$ and $O_3$ and Fraunhofer lines are correct.   Cloud interference is dominant over other parameters, and the cloud height and coverage must first be retrieved and corrected.   There are three methods to estimate cloud coverage.   One is to use different strength absorption.

47

Higher spectral resolution improves the accuracy, as described in the first part of this chapter, but a large spectrometer is necessary to meet his requirement. Another is to use the data of the imager that has higher spatial resolution than a spectrometer. The other method uses the scene-averaged albedo of the UV region, where the surface albedo is very small. The third method must assume cloud reflectivity, but no additional instrument is needed.

## (2) Filter radiometer

The theoretical studies indicate that a grating spectrometer, with medium spectral resolution is very sensitive to any distortion or shift in orbit. This is because the line shape function has a triangular or Gaussian shape and the $O_2$ $A$ band has the same line width. The spectrometer output is insensitive to the environment when the instrument line shape is much wider than the $O_2$ $A$ band spectra. The number of the spectral bands can be minimized if the information is limited to cloud height even considering the observation geometry. A filter radiometer with a flat spectral response is very robust. Recent coating technology enables the production of 5 nm bandwidth optical band-pass filters. Figure 3-13 illustrates the result of a cloud detection band simulation (air mass factor of 2) by MODTRAN and its sensitivity to the environment. The spectral characteristics of the narrow-band filters actually manufactured are depicted in Figure 3-14. The manufactured narrow-band pass filters ($O_2$-sensitive and -insensitive channels) and the expected output values of different solar zenith angle measurements on the ground are depicted in Figure 3-15. Table 3-4 reveal the sensitivity to the wavelength shift in the $O_2$ $A$ band region for rectangular and Gaussian shaped filters. The filter radiometer is very robust inn orbit if the filter has the ideal rectangular shape. The detailed design of these radiometers will be discussed in Chapter 4.
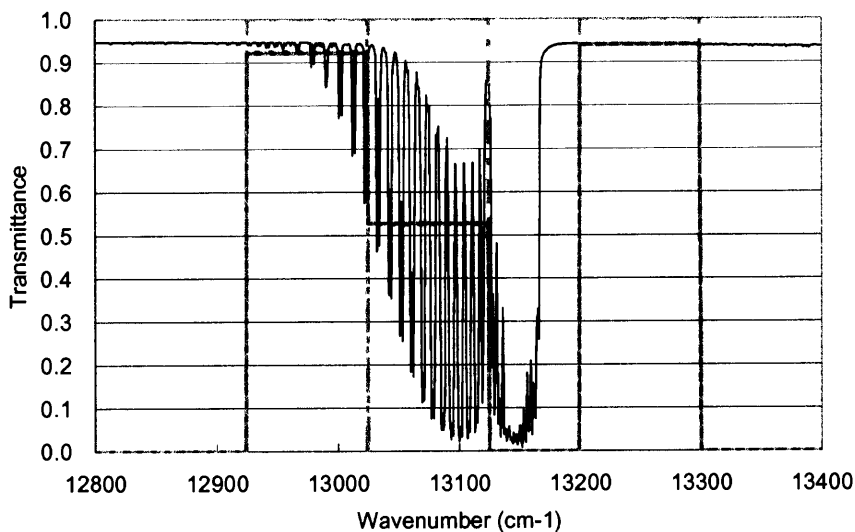
Figure 3-13. Cloud detection band outputs (air-mass factor of 2) and their sensitivity to the environment. The solid line, dash-dotted line, bold line, and dotted line represent the simulated absorption spectra, band pass filter spectral characteristics model, output of each channel and output for +/- 1 cm$^{-1}$ spectral shift.

48

Table 3-4.    Sensitivity to the wavelength shift in $O_2$ A band region: rectangular and Gaussian shape filter.

| Rectangular shape narrow bandpass filter | | | |
|---|---|---|---|
| | Ch 1 12975 cm$^{-1}$ | Ch 2 13075 cm$^{-1}$ | Ch 3 13250 cm$^{-1}$ |
| +1 cm$^{-1}$ | 0.06% | 0.04% | 0% |
| -1 cm$^{-1}$ | 0.4% | 0.23% | 0.01% |
| Gaussian shape narrow bandpass filter | | | |
| | Ch 1 | Ch 2 | Ch 3 |
| +1 cm$^{-1}$ | 0.1% | 0.5% | 0.1% |
| -1 cm$^{-1}$ | 0.2% | 0.5% | 0.01% |
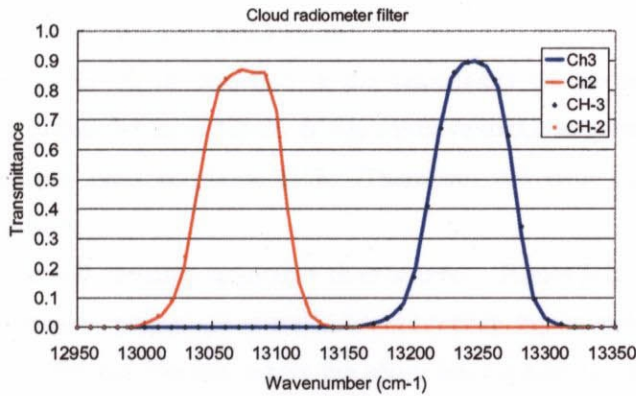


Figure 3-14.    Spectral characteristics of the manufactured narrow band filters.
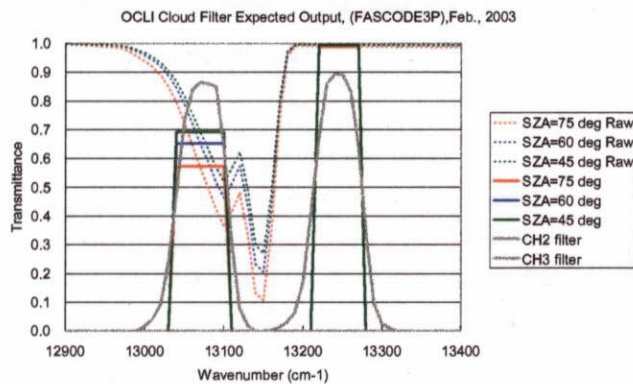


Figure 3-15.    Manufactured narrow band-pass filters ($O_2$ sensitive and insensitive channels) and the expected output values of different solar zenith angles measurements on the ground.

## (3) Radiative transfer calculation (look-up table) and cloud-height retrieval flow

The absorption of the $O_2$ isotope must be included in radiative transfer calculation, as shown above. Existing radiative transfer models with multiple scattering, such as MODTRAN does not have enough spectral resolution in this region.   Several absorption lines exist within one spectral channel.   The fine Fraunhofer line spectra, the absorption spectra of $O_2$, its isotope, and $O_3$, and the spectral response of the instrument (filter radiometer) must be convoluted and integrated with fine spectral steps for accurate radiance calculation. Cloud reflectivity and the vertical profile of temperature and pressure in terms of the latitude were modeled for multiple scattering calculations to prepare look-up tables (LUT).   The convoluted radiances of various cloud heights (for example 100 m steps) and the surface albedo are calculated before operation and stored as a LUT. Therefore, the LUT for each channel is a two-dimensional matrix of cloud height and surface albedo.

Radiative transfer out of the $O_2$ $A$ band depends on the aerosol extinction, surface albedo, and cloud reflectivity.   Effective surface albedo can be acquired using this channel.   Cloud coverage can be also estimated if a surface albedo global database is available and typical cloud reflectivity is assumed.   The cloud height can be estimated by comparing the convoluted radiance ratios in and out of the $O_2$ $A$ band with a pre-calculated LUT of the retrieved surface albedo value.

The major error source of cloud detection is the uncertainty of the temperature vertical profile. However, Figure 3-7 indicates that the line intensity is less sensitive to the temperature around 13080 $cm^{-1}$, the center of the strong absorption band in Figure 3-13.   Therefore, this error does not seriously affect the cloud-height estimation accuracy.

The surface albedo spectral variation is another error source.   Figure 3-16 depicts the U.S. Geological Survey (USGS) spectral library of plants: (a) overall UV and visible region and (b) around the $O_2$ $A$ band. There is a red edge between 700 and 750 nm, where the plants have a significant albedo difference, but it is relatively flat around the $O_2$ $A$ band.   Figure 3-17 shows the scattered light spectral data of different types of surfaces by FTS with 8 $cm^{-1}$ spectral resolution.   The scattered spectra over the grass surface exhibit no large spectral difference in either side of the $O_2$ $A$ band.   The error caused by surface albedo spectral variation is small if the filter has good out-of-band characteristics.



(a)

(b)
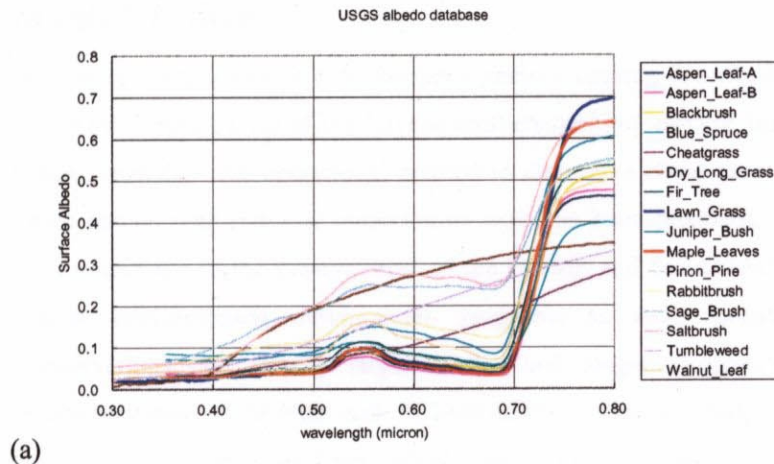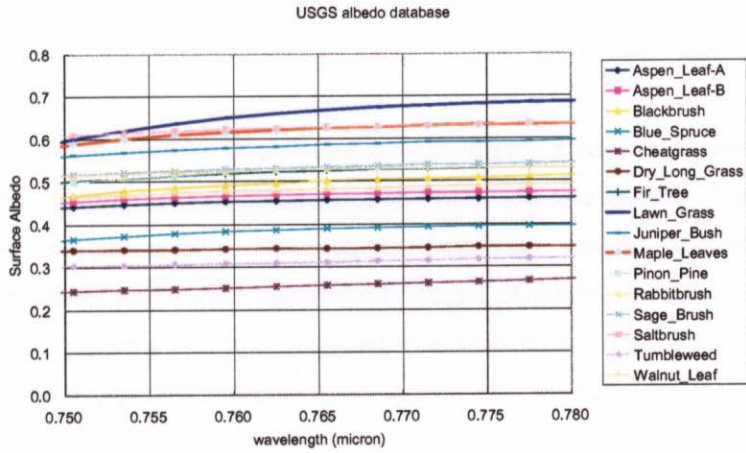
Figure 3-16.   USGS spectral library of the plants: (a) whole UV and visible region and (b) around $O_2$ $A$ band.
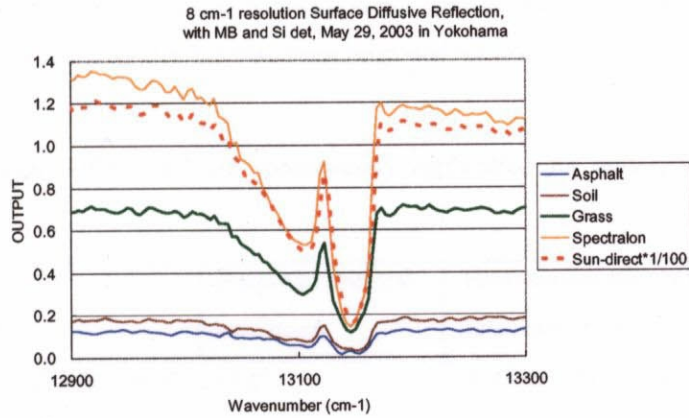


Figure 3-17.   Scattered light spectral of different types of surface by FTS with 8 cm$^{-1}$ spectral resolution.

## 3.7. Conclusion of this Chapter

The $O_2$ $A$ band spectroscopy application for atmospheric remote sensing described in this chapter is summarized in Table 3-5.   GOME and SCIAMACHY have several channels of varying, but moderate, optical depth in the $O_2$ $A$ and $B$ band regions.   An operational method to determine cloud parameters that has the potential to produce accurate results with minimal computation time has been proposed.   This method has been developed primarily to contribute to the development of the GOME and SCIAMACHY programs.   It may be effective for other satellite-based measurement programs as well, including geostationary meteorological satellite observations that employ larger IFOVs and longer integration times than the sun-synchronous satellite observations of GOME and SCIAMACHY.   Further studies of spectral band parameters and scattering effects including an Earth albedo study are required for accurate detection. Scattering studies currently underway include those of cloud-top reflection coefficients (BRDFs) coupled to

cloud type and altitude (J. Burrows, R. Spurr, and T. Kurosu, private communication, 1993) and the Monte Carlo multiple scattering calculations of scattering inside clouds (H. Frank and U. Platt, private communication, 1993).

A fine spectral resolution spectrometer is preferred for onboard $O_2$ $A$ band measurements for research purposes such as acquiring a line parameter database and solar Fraunhofer line spectra. Instrumentation of a balloon-borne spectrometer was discussed. However, the maximum spectral resolution available for nadir-looking application is greater than 1 $cm^{-1}$ due to the limitation of the target radiance. The maximum optical thickness for a 0.4 $cm^{-1}$ spectral resolution is about 5 as illustrated in Figure 3-18, while an optical thickness of 0.5, which is close to maximum sensitivity, is available for a 30 $cm^{-1}$ spectral resolution. This indicates that spectral resolution and sensitivity are not linearly proportional. Therefore, sufficient sensitivity can be achieved with relatively low spectral resolution by averaging the several absorption lines. A robust and optimized spectral-bandwidth filter radiometer or a grating spectrometer of moderate resolution is preferred since the spectral width and SNR can be modeled to be linearly proportional for operational purposes such as temperature and pressure retrieval or cloud-height detection. A compact filter radiometer for cloud detection for a next-generation UV spectrometer application will be discussed in Chapter 4 and Chapter 5. A moderate spectral resolution spectrometer has also been proposed for solar occultation mission.

Table 3-5. Summary of $O_2$ $A$ band spectroscopy application for atmospheric remote sensing.

| Application | Required spectral resolution | Error source except for instrument noise and error |
|---|---|---|
| Cloud coverage and height Retrieval (nadir looking, large IFOV)) or absolute column amount | High <1 $cm^{-1}$ | Surface albedo *a priori* information Temperature uncertainty (can be minimized using less sensitive band) |
| Temperature and pressure retrieval (solar occultation) | Moderate $\cong 10$ $cm^{-1}$ | Ray tracing of optical path between the sun, tangent point, and satellite (refraction effect) |
| Cloud height detection (nadir looking, small IFOV) | Low $\cong 100$ $cm^{-1}$ | Partial cloud condition Temperature uncertainty |
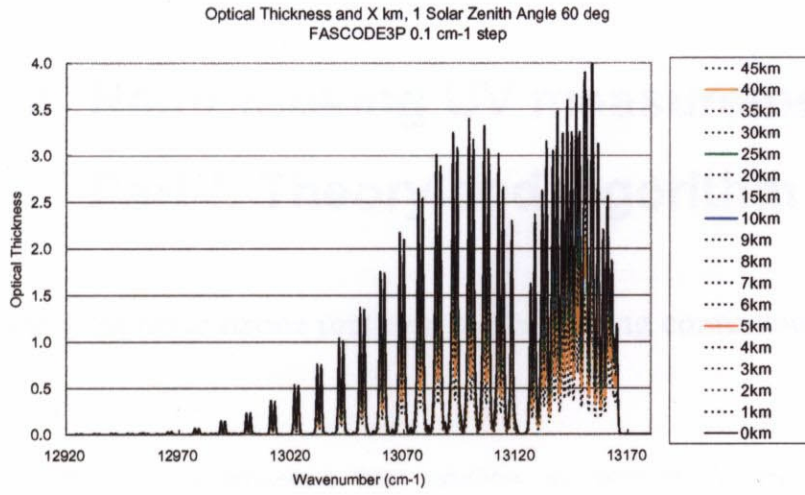
Figure 3-18.   Simulated optical thickness between outer space and cloud top height for the solar zenith angle of 60 deg and 0.4 cm$^{-1}$ spectral resolution.